

## Recent Increase of Spring Precipitation over the Three-River Headwaters Region—Water Budget Analysis Based on Global Reanalysis (ERA5) and ET-Tagging Extended Regional Climate Modeling<sup>©</sup>

SHASHA SHANG,<sup>a,b,c</sup> JOËL ARNAULT,<sup>c</sup> GAOFENG ZHU,<sup>b</sup> HUILING CHEN,<sup>b</sup> JIANHUI WEI,<sup>c</sup> KUN ZHANG,<sup>d,e</sup> ZHENYU ZHANG,<sup>c</sup> PATRICK LAUX,<sup>c,f</sup> AND HARALD KUNSTMANN<sup>c,f</sup>

<sup>a</sup> *Tianjin Key Laboratory of Water Resources and Environment, Tianjin Normal University, Tianjin, China*

<sup>b</sup> *Key Laboratory of Western China's Environmental Systems (Ministry of Education), College of Earth and Environmental Sciences, Lanzhou University, Lanzhou, China*

<sup>c</sup> *Institute of Meteorology and Climate Research (IMK-IFU), Karlsruhe Institute of Technology, Campus Alpin, Garmisch-Partenkirchen, Germany*

<sup>d</sup> *School of Biological Sciences, The University of Hong Kong, Hong Kong, China*

<sup>e</sup> *Department of Mathematics, The University of Hong Kong, Hong Kong, China*

<sup>f</sup> *Institute of Geography, University of Augsburg, Augsburg, Germany*

(Manuscript received 27 October 2021, in final form 11 July 2022)

**ABSTRACT:** Precipitation change is critical for the Three-River Headwaters (TRH) region, which serves downstream communities in East Asia. The spring (March–May) precipitation over the TRH region shows an increasing trend from 1979 to 2018, as revealed by a Chinese gridded precipitation product (CN05.1). However, the physical processes responsible for this precipitation change are still unclear. This study investigated the characteristics of spring precipitation and the water budget over the TRH region using the ERA5 global reanalysis and the Weather Research and Forecast (WRF) Model. The WRF version employed in this study includes online calculations of the atmospheric water budget and an evapotranspiration (ET) tagging procedure to trace evapotranspired water in the atmosphere. Both ERA5 and WRF reproduce the spring precipitation increase. Moreover, WRFD02 (with a 3-km domain) reduces the wet bias by around 60% and 77% compared to WRFD01 (9 km) and ERA5 (30 km). Both ERA5 and WRF demonstrate that the increase of spring precipitation is dominated by moisture convergence, especially the atmospheric water fluxes from the southern boundary. The enhanced moisture inflow is sustained by enhanced mass flux while the enhanced moisture outflow is sustained by increased moisture. The ET-tagging results further demonstrate the weakened precipitation recycling process because of the significant increase of precipitation produced by external moisture. Compared to ERA5, the reduced wet bias with WRF is attributed to a better spatial resolution of orographic barrier effects, which reduce the southerly water fluxes. The results highlight the potential of regional climate downscaling to better represent the atmospheric water budget in complex terrain.

**KEYWORDS:** Atmosphere; Atmosphere–land interaction; Hydrologic cycle; Climate variability; Regional models

### 1. Introduction

The Tibetan Plateau (TP) is the highest plateau in the world with more than half of its area over 4000 m and has been called the “third pole” (Qiu 2008). Compared to other regions at similar latitudes, the TP is more sensitive to global warming. The warming trend of the TP since the late 1980s is 1.5 times higher than the global warming rate (Liu and Chen 2000; Qin et al. 2009; Liu et al. 2009; Yang et al. 2014). This rapid warming can significantly accelerate the hydrological cycle, and thereby affect water resources and ecosystems in downstream regions (Immerzeel et al. 2010; de Oliveira et al. 2017; Xi et al. 2018; Liu et al. 2011). The Three-River Headwaters (TRH) region is located in the hinterland of the TP

and hosts the headwaters of the Yellow River, the Yangtze River, and the Lancang-Mekong River. The TRH region has a mean annual runoff of about  $500 \times 10^8 \text{ m}^3$  and is known as the “Asian water tower” (Shao et al. 2017; Zhang et al. 2012). Precipitation in the TRH region provides abundant water to the river systems in downstream regions, which dramatically influences ecosystems, agriculture, and water-related-sustainable development (Jiang et al. 2017; Jiang and Zhang 2016; Li et al. 2012; Zhang et al. 2012). Therefore, investigating the atmospheric water budget related to precipitation change over the TRH region is critical in climate research and adaptation policy.

Recent studies demonstrated that the TRH region has become warmer and wetter (Ji et al. 2020). Especially, winter and spring (cold season) precipitation has increased significantly since 1961 (Shi et al. 2016; Yi et al. 2013; Tong et al. 2014; Shang et al. 2021; You et al. 2012). The spring [March–May (MAM)] precipitation is relevant for the start of the growing season of vegetation, which affects the plant phenology and crop yield over the TRH region (Qian et al. 2010; Y. Zhang et al. 2017; Yan et al. 2020). Sun and Wang (2018) demonstrated that the

<sup>©</sup> Supplemental information related to this paper is available at the Journals Online website: <https://doi.org/10.1175/JCLI-D-21-0829.s1>.

Corresponding author: Gaofeng Zhu, zhugf@lzu.edu.cn

interannual variability of spring precipitation over the TRH region is modulated by anomalous easterly and southerly water vapor transport associated with the La Niña SST pattern. More recently, Shang et al. (2021) indicated that the increased cold season precipitation over the TRH region from 1961 to 2014 is associated with enhanced southeasterly water vapor transport, which is possibly related to the enhanced Walker circulation. In addition, along with rapid warming over the TP and changes in the climate and atmospheric circulations, the hydrological cycle is also altered. Yan et al. (2020) have analyzed the annual and seasonal atmospheric water budget and its long-term trend over the whole TP based on the ERA5 reanalysis data. They proposed that the decrease of outside water vapor transport and increase in evapotranspiration (ET) in the TRH region may result in the depletion of surface water storage during the summer season. Their results also show an increase in spring precipitation over the TRH region from 1979 to 2018, but a detailed atmospheric water budget analysis for this region was not performed. Exploring the variation of atmospheric water budget components in this region can enhance our understanding of the physical processes responsible for the increase of spring precipitation.

The calculation of atmospheric water budgets can potentially be done using global atmospheric reanalysis, but this approach has limitations (Hagemann et al. 2005; Trenberth and Guillemot 1998; Trenberth et al. 2007). For example, Cullather et al. (2000) demonstrated that the annual  $P - E$  values from the NCEP–NCAR and ECMWF analyzed fields are lower than those obtained from moisture flux convergence by about 60%. Model configuration and data assimilation techniques are key factors affecting the quality and stability of reanalysis (Dee et al. 2011; Seager and Henderson 2013). The performance of global atmospheric reanalysis on the local scale also has to be treated with caution, as the assessment of the moisture budget balance at regional scales is more challenging than at the global scale (Brown and Kummerow 2014), especially in steep terrain regions such as the TP. Compared with global atmospheric models, dynamical downscaling models have emerged with improved parameterizations of physical processes, such as the Weather Research and Forecasting (WRF) Model (Skamarock and Klemp 2008). In particular, the refined land surface and terrain information in regional climate models (RCMs) can lead to an improved representation of the moisture flux dynamics and budgets (Castro et al. 2005). For the TP, numerous studies have demonstrated that the high-resolution RCMs could improve precipitation simulation over complex terrain (Collier et al. 2013; Mughal et al. 2017; Karki et al. 2017). However, few studies explore the added value of dynamical downscaling with RCMs for the representation of atmospheric water budget over the high-altitude mountain area. Therefore, this study attempts to analyze the atmospheric water budget with both global reanalysis (ERA5) and a downscaling model (WRF).

The precipitation over a land region is composed of two components: the advective external component resulting from the fluxes of water vapor into the region and the internal component resulting from local evapotranspiration (Burde and Zangvil 2001). The precipitation recycling ratio, defined as the contribution rate of the local evapotranspiration to the

total precipitation, is an important indicator for understanding the change of land–atmospheric interactions in the context of the changed atmospheric branch of the hydrological cycle. The precipitation recycling can be assessed with a tagged procedure within an RCM (Arnault et al. 2016; Zhang et al. 2019; Wei et al. 2015; Knoche and Kunstmann 2013; Arnault et al. 2019, 2021; Gao et al. 2020; Yang and Dominguez 2019; Dominguez et al. 2016; Insua-Costa and Miguez-Macho 2018).

This paper aims to conduct the regional atmospheric water budget analysis combined with the global ERA5 reanalysis data and the regional-scale WRF simulations to better understand the physical processes leading to spring precipitation variability in the TRH region over the past decades. Moreover, we intend to evaluate the changes of the contribution from surface evapotranspiration to precipitation in spring over the TRH region to quantify the response of the land–atmospheric interaction to the increased spring precipitation. The specific objectives of this study are 1) to investigate the performance of the ERA5 reanalysis data and the WRF model in the simulated spring precipitation change from 1979 to 2018 over the TRH region, 2) to explore the change of the atmospheric water budget components corresponding to the changed spring precipitation in the study region using the ERA5 reanalysis and the WRF model, 3) to understand the added value of the WRF model compared to the global reanalysis in the atmospheric water budget description over the TRH region, and 4) to quantify the change of land–atmosphere interactions by applying the ET-tagging method embedded in the WRF model.

## 2. Model configuration, datasets, and methodology

### a. Study region

The TRH region is located in southern Qinghai Province, China. It supplies about 25%, 15%, and 49% of the total runoff for the Yangtze River basin, the Yellow River basin, and the Mekong River basin, respectively (Zhang et al. 2012). The altitude of the TRH region ranges from 3335 to 6564 m (Fig. 1). The landscape of the TRH region is dominated by glaciers, snow cover, permafrost, and wetlands (Tong et al. 2014; Wang et al. 2022). The climate is modulated by the East Asian monsoon and the prevailing westerlies (Yang et al. 2014). The annual temperature ranges between  $-5.6^{\circ}$  and  $7.8^{\circ}\text{C}$ , and the annual precipitation is between 262 and 772 mm (Yi et al. 2013). The mainland cover types are grassland and open shrubland as shown in Fig. 1b.

### b. Model configuration

The WRF Model is a mesoscale numerical weather prediction system (Skamarock et al. 2008). It is a nonhydrostatic model with several available dynamic cores, which can be used for a wide variety of applications, and scales ranging from the global scale to large-eddy simulations. It contains several parameterization options for microphysics, longwave and shortwave radiation, the planetary boundary layer, cumulus clouds, and the land surface. The dynamical core of the Advanced Research WRF in version 4.0 is used in this study.

To simulate the climate variables with WRF over the TRH region, the two domains shown in Fig. 1a are used. The model

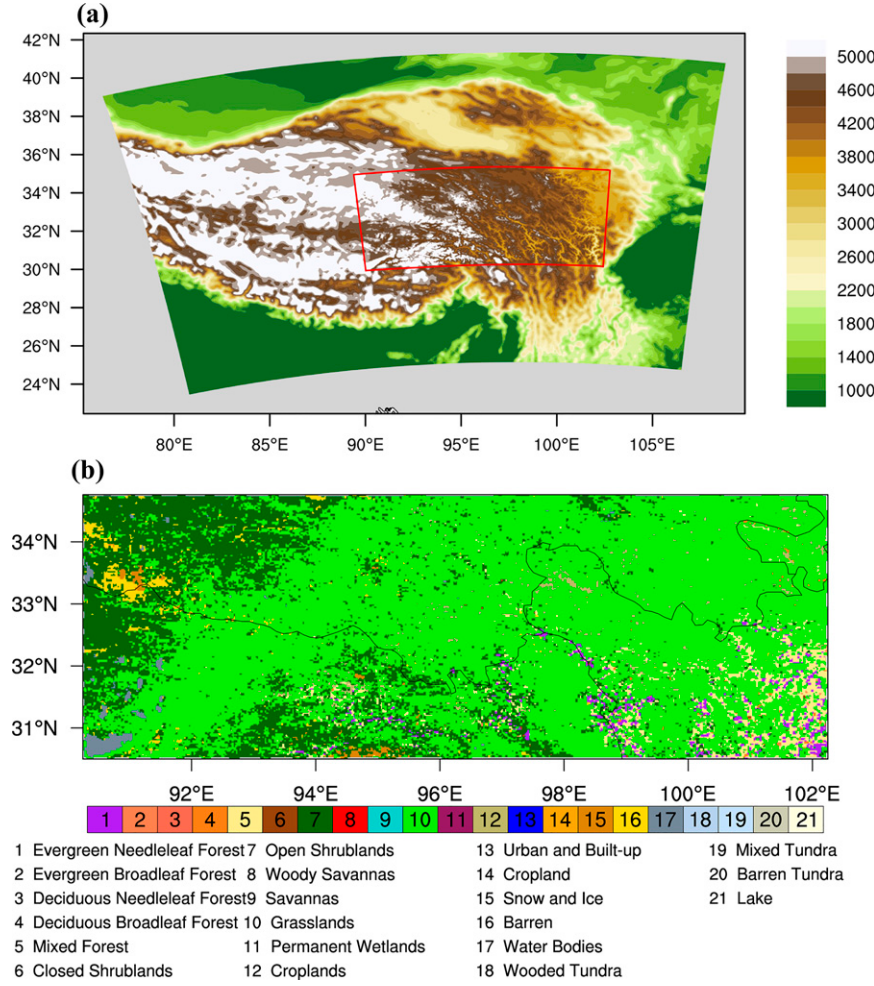


FIG. 1. (a) Geographical location of the Three-River Headwaters (TRH) region and also the terrain elevation of the simulation's domains; color denotes the terrain height of the parent domain (d01) and the inner domain (d02) in the WRF simulation (m). The red rectangle in (a) denotes the location of d02. (b) The analyzed region in this study and land cover types.

is applied following a one-way nesting approach with two domains (Fig. 1) driven by ERA5 initial conditions and lateral boundary conditions. WRF is set up with a 9-km horizontal grid spacing with  $300 \times 200$  horizontal grid points for domain 1 (centered at  $33^{\circ}\text{N}$ ,  $93^{\circ}\text{E}$ ), covering the major TP (Fig. 1a), and a 3-km horizontal grid spacing with  $400 \times 187$  horizontal grid points for the domain 2, focusing on the TRH region. Taking into account the WRF Lambert projection and also to eliminate the effect of the relaxation zone, the analyzed area in this study is  $30.25^{\circ}$ – $34.75^{\circ}\text{N}$ ,  $90.25^{\circ}$ – $102.25^{\circ}\text{E}$  as shown in Fig. 1b. Vertical levels are set to 40 levels from the near surface up to 20 hPa, using a time step of 45 s. The schemes selected for this study are listed in Table 1.

### c. Experimental design

Twenty model runs covering a 6-month period each, from 1 January to 1 June, are considered, 10 for the so-called dry period from 1979 to 1988 and 10 for the so-called wet period

from 2009 to 2018. The model is reinitialized every year on 1 January. For each year simulation, the first two months are considered as a spinup period and the last three months are the study period.

The WRF-based ET-tagging method from Arnault et al. (2016) is also used. The tagged atmospheric water variables are initially set to zero and the land surface evapotranspiration

TABLE 1. Physical schemes of the WRF model used in this study.

Subject	Select option	Reference
Shortwave radiation	Dudhia	Dudhia (1989)
Longwave radiation	RRTM	Mlawer et al. (1997)
Microphysics	WSM6	Hong et al. (2006)
Cumulus parameterization	Domain 1 KF; domain 2 none	Kain and Fritsch (1992)
Planetary boundary layer	Yonsei University (YSU)	Hong et al. (2006)
Land surface model	Noah-MP	Niu et al. (2011)

occurring over the simulation's domain 2, which is our study region, is treated as the source of tagged water vapor. The skill of the model in correctly representing the atmospheric process and land-atmosphere process occurring in the study region is assessed by comparing the simulated precipitation and land surface evapotranspiration with gridded datasets.

#### d. Datasets

##### 1) GRIDDED REFERENCE DATA FOR MODEL VALIDATION

To analyze the spring precipitation variability over the TRH region and evaluate the performance of WRF in our study region, the gridded daily CN05.1 precipitation dataset is used. This gridded dataset is constructed from daily records of 2472 rain gauges in China at a resolution of  $0.25^\circ \times 0.25^\circ$  from 1961 to 2018 (Wu and Gao 2013). The CN05.1 data have been widely used to investigate regional climate change and validate high-resolution climate models (e.g., Shi et al. 2018; Shang et al. 2021). The daily evapotranspiration from the Global Land Evaporation Amsterdam Model (GLEAM) version 3.5a was used as the reference ET data, which is based on satellite and reanalysis data spanning the 41 years from 1980 to 2020 with a spatial resolution of  $0.25^\circ$  globally (Martens et al. 2017; Miralles et al. 2011).

##### 2) GLOBAL REANALYSIS FOR ATMOSPHERIC WATER BUDGET ANALYSIS AND INITIAL AND LATERAL BOUNDARY CONDITION FOR THE WRF MODEL

Analysis of the atmospheric water budget relies on detailed information about variations in winds and humidity. Such data are typically available from global atmospheric reanalyses like the NCAR-NCEP (Kalnay et al. 1996), ECMWF ERA-40 (Uppala et al. 2005), ECMWF ERA-Interim (Dee et al. 2011), and ECMWF ERA5 (Hersbach et al. 2018). The new fifth-generation European Centre for Medium-Range Weather Forecasts Reanalysis (ERA5; Hersbach et al. 2018) is used for the atmospheric moisture budget analysis in this study. ERA5 is the most recent reanalysis dataset of ECMWF; it embodies detailed records of the global atmosphere and land surface from 1950 onward and replaces the ERA-Interim dataset. The spatial resolution has been increased to  $\sim 31$  km ( $0.25^\circ$ ) with 137 vertical layers. Besides the higher resolution, ERA5 also benefits from an improved data assimilation system, hourly output, uncertainty estimates, and a large variety of output parameters (Hersbach et al. 2018). The atmospheric moisture budget fields of ERA5 (precipitation, evapotranspiration, vertically integrated moisture divergence, and total column atmospheric water) are used at the highest available spatial (31 km) and temporal (hourly) resolution. ERA5 also provides initial and lateral boundary conditions for WRF simulations. The temporal storage interval of the ERA5 for driving WRF is 6 h at 0000, 0600, 1200, and 1800 UTC. For evaluation, the precipitation and evapotranspiration from WRF and ERA5 are remapped to the CN05.1 data and the GLEAM data by bilinear interpolation.

#### e. Methods

##### 1) ATMOSPHERIC WATER BUDGET

The calculation of the moisture budget is based on the balanced equation for atmospheric water (Seager and Henderson 2013). The atmospheric water budget is given by

$$\frac{\partial W}{\partial t} - \nabla \cdot \mathbf{Q} = P - ET + \text{residual}, \quad (1)$$

where  $W$  and  $-\nabla \cdot \mathbf{Q}$  denote the atmospheric water storage and the moisture convergence, and the residual term refers to the model bias (Seager et al. 2010; Trenberth and Guillemot 1995; Seager and Henderson 2013). The vertical integral of moisture convergence is defined by

$$-\nabla \cdot \mathbf{Q} = -\frac{1}{g} \nabla \cdot \int_{p=0}^{p=p_s} \mathbf{V} q \, dp, \quad (2)$$

with air pressure  $p$  (Pa), gravitational acceleration  $g$  ( $\text{m s}^{-2}$ ), horizontal wind vector  $\mathbf{V}$  ( $\text{m s}^{-1}$ ), and specific humidity  $q$  ( $\text{kg kg}^{-1}$ ). At seasonal time scales, the variations of the atmospheric water storage  $W$  can be assumed to be negligible (Peixto and Oort 1984), which leads to the following simplified budget equation:

$$P = ET - \nabla \cdot \mathbf{Q} + \text{residual}. \quad (3)$$

This atmospheric water budget is calculated “offline” with the hourly ERA5 outputs. In WRF this budget is calculated “online” using the method of Arnault et al. (2016), so that in this case the budget components are directly provided in the WRF outputs.

The moisture budget can be decomposed according to Seager et al. (2010) as follows:

$$\rho_w g(P - ET) = - \int_{p=0}^{p=p_s} (\bar{\mathbf{V}} \cdot \nabla \bar{q} + \bar{q} \nabla \cdot \bar{\mathbf{V}}) \, dp - \int_{p=0}^{p=p_s} \nabla \cdot (\bar{\mathbf{V}}' q') \, dp - q_s \mathbf{V}_s \cdot \nabla p_s, \quad (4)$$

where overbars indicate monthly means and primes indicate the departure from monthly mean,  $p$  is pressure,  $q$  is specific humidity,  $\mathbf{V}$  is the horizontal vector wind,  $\rho_w$  is the density of water, and the subscript  $s$  represents surface values.

To understand the potential mechanisms governing the precipitation change between the dry period and the wet period, we denote

$$\delta(\cdot) = (\cdot)_{\text{wet}} - (\cdot)_{\text{dry}} \quad (5)$$

where subscripts “wet” and “dry” indicate the values of the arbitrary quantity in parentheses during the wet period and the dry period. Then Eq. (4) can be approximated as follows:

$$\begin{aligned} \rho_w g(P - ET) \approx & - \int_{p=0}^{p=p_s} (\delta \bar{\mathbf{V}} \cdot \nabla \bar{q}_{\text{dry}} + \bar{\mathbf{V}}_{\text{dry}} \cdot \nabla \delta \bar{q} \\ & + \delta \bar{q} \nabla \cdot \bar{\mathbf{V}}_{\text{dry}} + \bar{q}_{\text{dry}} \nabla \cdot \delta \bar{\mathbf{V}}) \, dp \\ & - \int_{p=0}^{p=p_s} \nabla \cdot \delta (\bar{\mathbf{V}}' q') \, dp - \delta(q_s \mathbf{V}_s \cdot \nabla p_s). \end{aligned} \quad (6)$$

In Eq. (6), terms involving changes in  $q$  but not changes in  $\mathbf{V}$  are referred to as the thermodynamic contribution to changes  $P - ET$ , terms involving changes in  $\mathbf{V}$  but no changes in  $q$  as the dynamic contribution.

Here, we only consider the contribution of mean flow for moisture transport. The moisture convergence can be broken down as follows:

$$\delta TH = - \int_{p=0}^{p=p_s} \nabla \cdot (\mathbf{V}_{dry} [\delta \bar{q}]) dp \quad (7)$$

$$\delta MCD = - \int_{p=0}^{p=p_s} \nabla \cdot ([\delta \bar{\mathbf{V}}] \bar{q}_{dry}) dp \quad (8)$$

where  $\delta TH$  and  $\delta MCD$  represent the contribution of thermodynamic and mean dynamic circulations for the moisture convergence.

The area-averaged moisture transport can be calculated by two methods, either the divergence field of atmospheric water fluxes over a specific region or by the input/output of the atmospheric water fluxes through four lateral boundaries of this region. For the second method, the moisture transported through each boundary  $Q_b$  is calculated following the method from Schmitz and Mullen (1996):

$$Q_b = \int_L \mathbf{Q} \times \mathbf{n} dl, \quad (9)$$

where  $\mathbf{n}$  represents the inward unit vector normal to the corresponding boundary and  $L$  is the length of the boundary. For the area average moisture transport, the formulation becomes

$$-\nabla \cdot \mathbf{Q} = \frac{1}{A} \left( \int_{L_w} \mathbf{Q}_u \times \mathbf{n} dl - \int_{L_E} \mathbf{Q}_u \times \mathbf{n} dl + \int_{L_s} \mathbf{Q}_v \times \mathbf{n} dl - \int_{L_N} \mathbf{Q}_v \times \mathbf{n} dl \right), \quad (10)$$

where  $\mathbf{Q}_u$  and  $\mathbf{Q}_v$  represent the zonal and meridional components of the integrated water fluxes. Theoretically, both methods lead to the same results, although time sampling approximations in offline calculation can introduce some numerical discrepancies between the two formulations (Li et al. 2013).

The boundary fluxes and the decomposition of the water budget are calculated by the 6-hourly ERA5 outputs formed into monthly means and the hourly outputs from WRFD01 (using variables of  $u$  winds,  $v$  winds, and specific humidity).

## 2) WRF-BASED ET-TAGGING METHOD

The ET-tagging method is an online diagnostic method to trace moisture that originates as evapotranspiration from the source region until it reaches the lateral boundary of the simulation's domain or falls as precipitation (Arnault et al. 2016; Wei et al. 2015; Knoche and Kunstmann 2013; Yang and Dominguez 2019; Sodemann et al. 2009; Zhang et al. 2019). This method consists of considering a second numerical formulation of the atmospheric hydrological cycle in the RCM for the tagged water, as elaborated by Knoche and Kunstmann (2013)

in the MM5 model and recently implemented in the WRF model (Arnault et al. 2016; Zhang et al. 2019; Arnault et al. 2021). Evaporated water from a selected region will be "tagged" when entering the atmosphere. This means that each water variable has a corresponding tagged water variable, and each equation describing the fate of a water variable has a corresponding equation describing the fate of the corresponding tagged water variable. The tagged water is numerically treated in the physical processes as the total moisture in the simulation which undergoes the same transport process and phase changes. To do this, there is an approximation that the tagged water is fully mixed so that processes acting on tagged water are simply scaled with a tagged water ratio.

## 3) PRECIPITATION RECYCLING RATIO

The contribution of land surface evapotranspiration to precipitation, namely the regional precipitation recycling (Brubaker et al. 1993), is assessed with the WRF-based tagging procedure (Arnault et al. 2016). Precipitation recycling ratio has been widely used for characterizing the regional water cycle and land-atmosphere interaction strength (Gao et al. 2020; Zhang et al. 2022), and is calculated as follows:

$$\rho = \frac{P_{tag}}{P_{total}}, \quad (11)$$

where  $P_{tag}$  denotes the tagged precipitation originating from ET in the source region, while  $P_{total}$  denotes the total precipitation. The  $P_{tag}$  is a measure of the regional precipitation recycling occurring in the source region.

In addition, the Student's  $t$  test is used to assess the statistical significance of the spatial difference between the wet period and the dry period.

## 3. Results and discussion

### a. Spatiotemporal change of spring precipitation

Figure 2a shows the long time series of standardized spring precipitation from 1979 to 2018 based on ERA5 and CN05.1 over the TRH region. The observations show large positive anomalies almost every year after 2000, while negative anomalies are observed before 2000. It reveals a dry-to-wet shift at the beginning of the 2000s. The observations show that the spring precipitation increased from 1979 to 2018 at a rising ratio of  $0.07 \text{ mm day}^{-1} \text{ decade}^{-1}$ , which is statistically significant at 99% confidence level (Fig. 2b). To investigate the change of spring precipitation over the TRH region, two sub-periods, namely a relatively dry period from 1979 to 1988 (10 continuous years) and a comparable wet period from 2009 to 2018 (10 continuous years), are selected based on the observations. The spring precipitation amount is less than  $1 \text{ mm day}^{-1}$  almost every year (except in 1981, 1985, and 1988) during the dry period, whereas it is more than  $1 \text{ mm day}^{-1}$  ( $1.1 \text{ mm day}^{-1}$ ) during the wet period (see Table 1 in the online supplemental material). The significance of the precipitation difference between the dry period and the wet period is tested by the paired-samples  $t$  test. The result shows that the

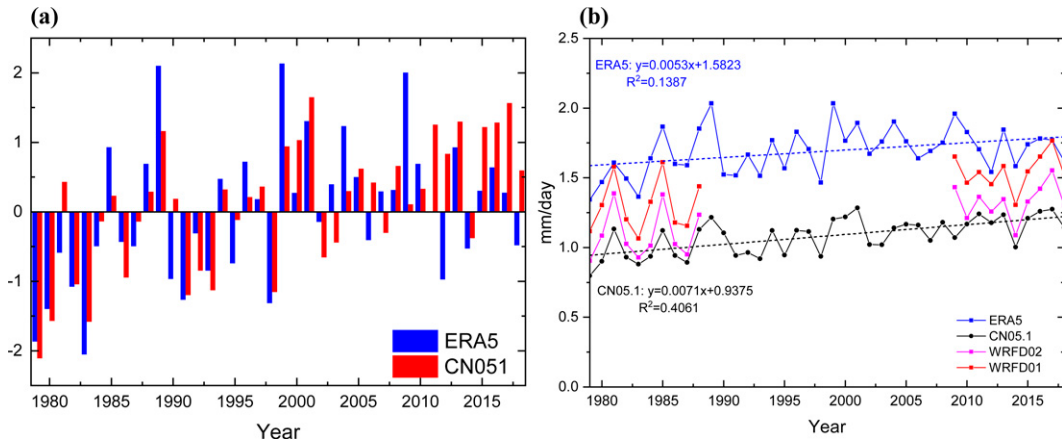


FIG. 2. (a) Time series of standardized spring precipitation over the TRH region from 1979 to 2018 based on ERA5 and CN05.1 and (b) time series of spring precipitation amount from 1979 to 2018 based on ERA5, CN05.1, WRF01, and WRF02 [1979–88 (10 years) and 2009–18 (10 years)].

difference is statistically significant at the 99% confidence level. It implies the evidenced wetting trend in spring over the TRH region, and the pattern has been recurrent in the recent decade. Li et al. (2021) show that the runoff of the Yangtze River in June increased after 1990, which may be a response to the increased precipitation in spring.

The correlation coefficient between the standardized spring precipitation based on ERA5 and CN05.1 is 0.7 and statistically significant at the 99% confidence level, which indicates that ERA5 captures the rising trend of the spring precipitation similar to the observations. Nevertheless, ERA5 highly overestimates the spring precipitation amount (about  $0.6 \text{ mm day}^{-1}$ ) compared with observations (Fig. 2b). The calculated linear trend from ERA5 is  $0.05 \text{ mm day}^{-1} \text{ decade}^{-1}$ , which is statistically significant at the 95% confidence level. To examine whether the increase of the spring precipitation based on ERA5 is entirely defined by only one year (e.g., 2009), the mean spring precipitation excluding the year 2009 is calculated, and the value is  $1.59 \text{ mm day}^{-1}$ , which still reveals the wetting during the wet period.

The spring precipitation during the dry and wet periods is also simulated with the WRF model. The WRF results still show a wet bias [about  $0.35 \text{ mm day}^{-1}$  with WRF for domain 1 (WRF01) and  $0.14 \text{ mm day}^{-1}$  for domain 2 (WRF02)]. This can be seen as a usual model discrepancy over the TP (e.g., Gao et al. 2014, 2015, 2018). However, the WRF02 result outperforms WRF01 and ERA5 by reducing the wet bias by around 60% and 77% separately. The topographical fields of ERA5, WRF01, and WRF02 are presented in Fig. 3. A better definition of topography in WRF02 than in WRF01 and ERA5 is evident. Downscaling can effectively improve precipitation accuracy due to resolving small-scale physical processes (Zhou et al. 2021; Xu et al. 2018; Wang et al. 2020; Gao et al. 2015, 2014; Shi et al. 2018).

The mean precipitation simulated by the WRF model (WRF02) is  $1.08$  and  $1.33 \text{ mm day}^{-1}$  during the dry and wet periods. The difference of precipitation between the dry period and the wet period simulated by WRF is statistically

significant at the 99% confidence level, which indicates that WRF also reproduces the increase of the spring precipitation reasonably in time. The daily precipitation validation shows that the overestimation in the WRF model is more pronounced for heavy precipitation (Fig. S1) (Gao et al. 2018), which may be a reason for even larger overestimations during relative wet years (Fig. 2b). Nevertheless, ERA5 and WRF both reproduce the wetting trend of spring precipitation in recent years over the TRH region.

Figures 4a and 4b show the spatial pattern of mean spring precipitation based on CN05.1 during the dry and wet periods. Spring precipitation over the TRH region shows a gradient

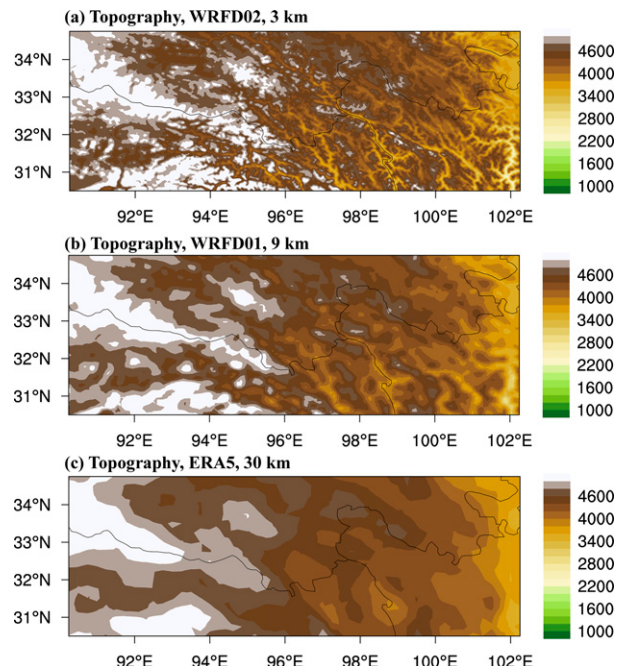


FIG. 3. Topography (m) over the TRH region represented by (a) WRF02\_3 km, (b) WRF01\_9 km, and (c) ERA5\_30 km.

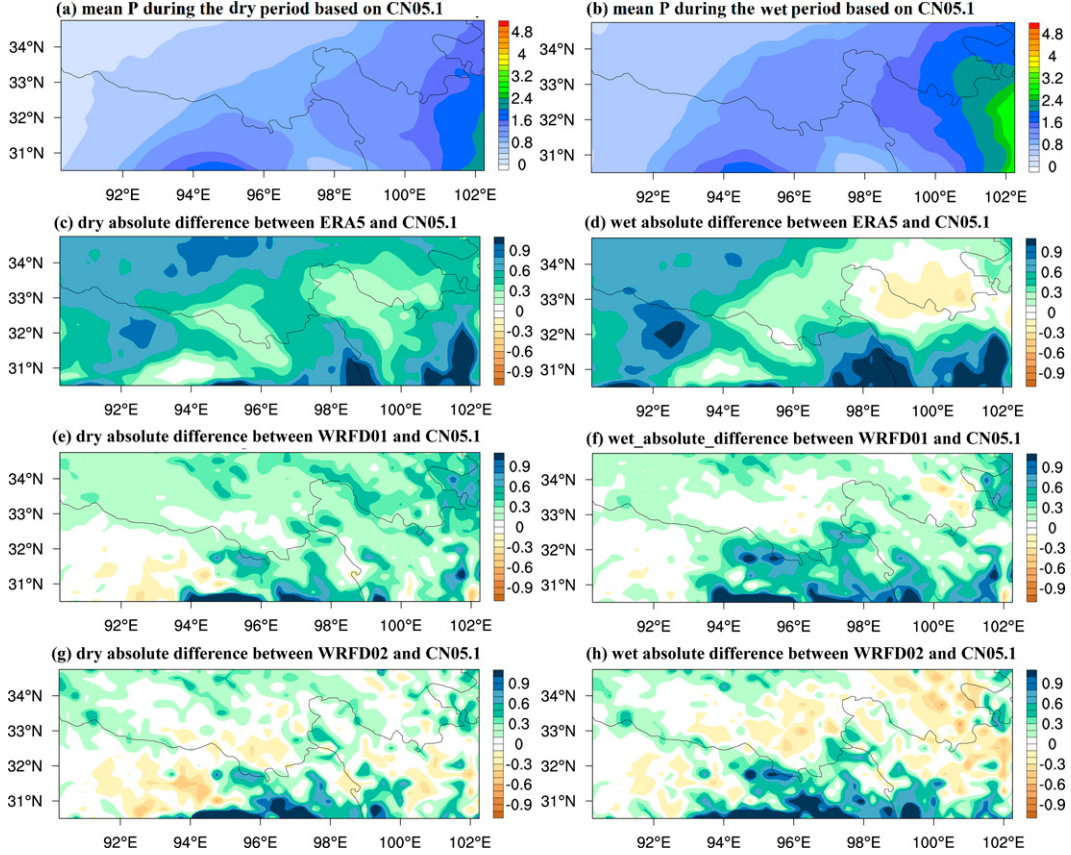


FIG. 4. Spatial pattern of mean spring precipitation ( $\text{mm day}^{-1}$ ) based on CN05.1 during the (a) dry and (b) wet periods; absolute difference of spring precipitation between ERA5 and CN05.1 during the (c) dry and (d) wet periods. (e)–(h) As in (c) and (d), but with WRFD01 and WRFD02.

from southeast to northwest with more precipitation in southeastern TRH and less precipitation in the northwestern TRH. Figures 4c–h show the absolute difference between ERA5, WRFD01, and WRFD02 and CN05.1 during the dry and wet periods. ERA5 overestimates the spring precipitation both for the dry and wet periods, especially in the southeastern region (more than  $1 \text{ mm day}^{-1}$ ) and the northwestern TRH region where the altitude is the highest (Fig. 3; Ji and Kang 2013; Zhou et al. 2021; Wang et al. 2020). The differences between WRF and CN05.1 are smaller than ERA5 (Figs. 4e–h). WRFD01 overestimates spring precipitation in the northeastern TRH region (about  $0.3 \text{ mm day}^{-1}$ ) and the central south edge (more than  $0.7 \text{ mm day}^{-1}$ ). Wet biases are reduced more in WRFD02 except for the central south edge similar to the parent domain. Besides, the WRFD02 simulation produces a few dry biases over the northeastern region during the wet period. In total, the WRF model outperforms the ERA5 very much in terms of precipitation wet bias, potentially because of the higher spatial resolution (3-km high-resolution grid) compared to the ERA5 global reanalysis (Zhou et al. 2021), which allows for a more realistic representation of moist convection processes in complex terrain (Fig. 3).

Figures 5a and 5b show the spatial pattern of mean evapotranspiration based on GLEAM data during the dry and wet

periods. Similar to precipitation, evapotranspiration also increases from the southeast to the northwest. The evapotranspiration of ERA5 is close to the GLEAM data except for a small overestimate in northwestern TRH during the dry period. The overall bias of evapotranspiration simulated by WRF is also low except for an overestimate in the central and eastern TRH and dry bias in the western region, especially during the wet period. WRFD02 performs a bit better compared to WRFD01. The relatively good agreement of precipitation and evapotranspiration between the WRF model and observations suggests that the model setup in this study is suitable for representing the characteristics of the atmospheric water budget and land-atmosphere interactions over the TRH region.

Figure 6 shows the average monthly precipitation during the dry and wet periods based on CN05.1, ERA5, and WRF. It shows that ERA5 always overestimates the precipitation of more than  $0.5 \text{ mm day}^{-1}$  for every month, during both the dry and wet periods. The WRF model results (both WRFD01 and WRFD02) show comparatively good agreement with the observation data in March (wet bias less than  $0.1 \text{ mm day}^{-1}$ ). The largest wet bias occurs in May when the South Asia summer monsoon onset leads to strong remote water vapor transport, but the topographic drags in the model result in excessive water vapor transport (Beljaars et al. 2004; Wang et al.

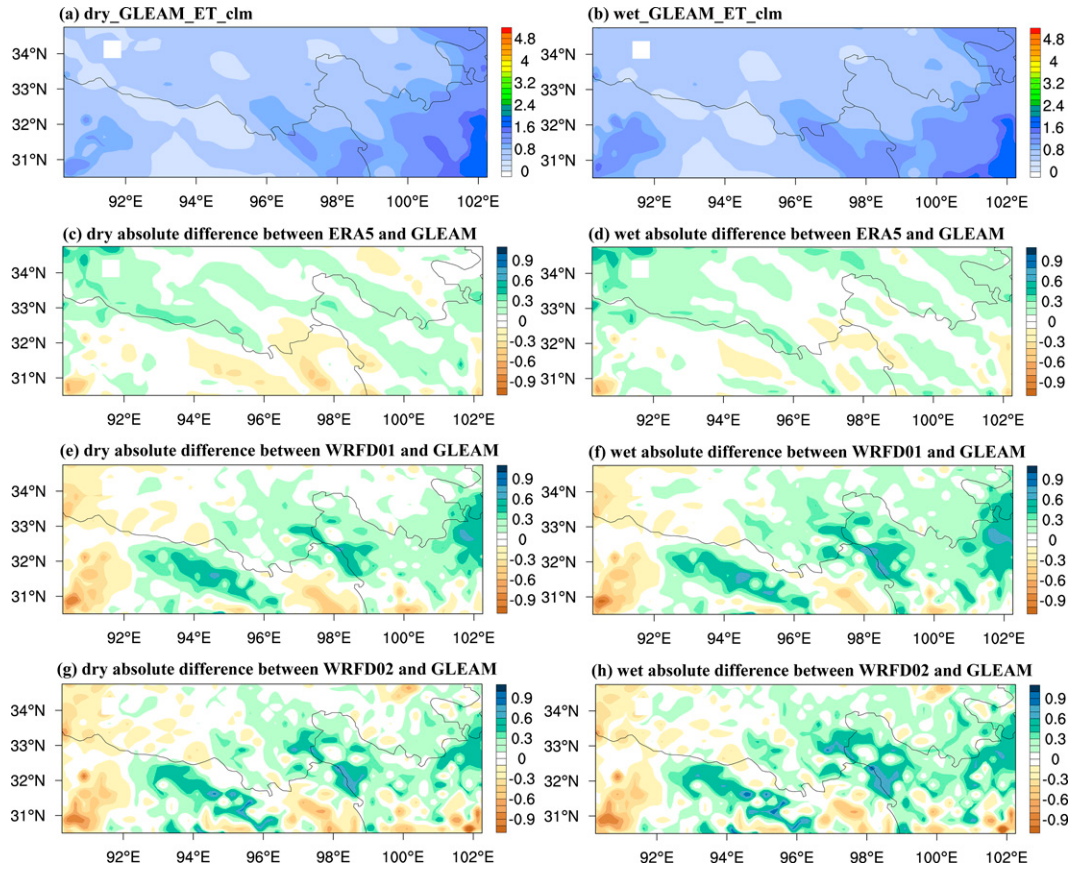


FIG. 5. Spatial pattern of mean spring evapotranspiration ( $\text{mm day}^{-1}$ ) based on GLEAM during the (a) dry period and (b) wet period; absolute difference of spring evapotranspiration between ERA5 and GLEAM during the (c) dry period and (d) wet period. (e)–(h) As in (c) and (d), but with WRF.

2020). This is also the reason why the wet bias of WRFD01 is larger than WRFD02 (Fig. 3). Nevertheless, the WRF model, especially the results from the nested domain, still outperforms ERA5 for the representation of precipitation in monthly scales because of the high resolution (Fig. 3).

Figure 6c shows the differences in monthly precipitation in spring between the wet and the dry periods from CN05.1, ERA5, and WRF, respectively. The WRF model shows a higher (smaller) difference in precipitation compared to the observations in May (April). It is noted that the difference

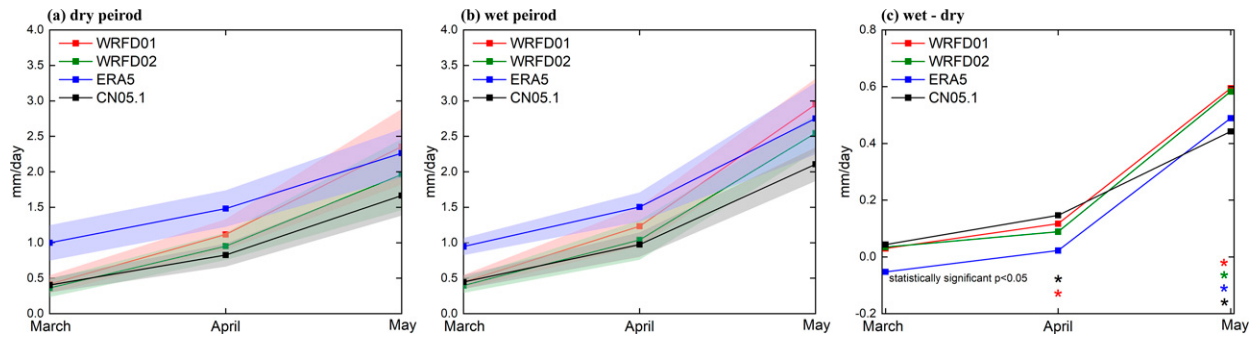


FIG. 6. Comparison of monthly precipitation during (a) the dry period (1979–88) and (b) the wet period (2009–18) based on CN05.1, ERA5, WRFD01, and WRFD02; (c) time series of monthly precipitation difference between the wet and dry periods based on CN05.1, ERA5, WRFD01, and WRFD02. The shadows indicate the standard deviation of the mean value. The asterisks (\*) with different colors represent that the differences of the respective variables between the dry period and the wet period in every month are statistically significant at the 95% confidence level.

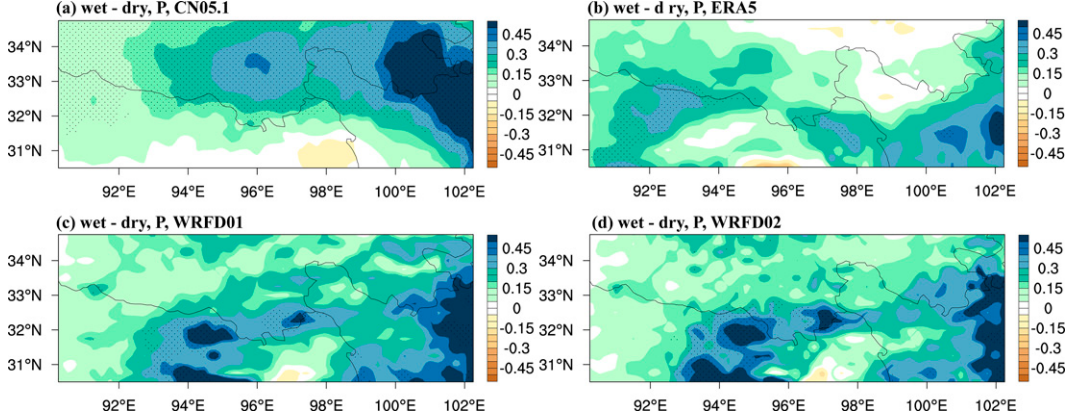


FIG. 7. Spatial pattern of the differences of spring precipitation ( $\text{mm day}^{-1}$ ) between the wet period (2009–18) and the dry period (1979–88) based on (a) CN05.1, (b) ERA5, (c) WRFD01, and (d) WRFD02. Dotted regions indicate that differences are statistically significant at the 95% confidence level.

presented by the parent domain and nested domain is almost the same. Nevertheless, the WRF model, ERA5, and the observations all demonstrate the highest precipitation increase in May during the South Asian summer monsoon onset. The remarkable increase of precipitation in May from 1979 onward over the southeastern TP has been reported in other studies, which suggests that it may be related to the earlier onset of the South Asian summer monsoon (e.g., [W. Zhang et al. 2017](#)).

[Figure 7a](#) shows the spatial pattern of the difference of spring precipitation between the wet period and the dry period based on CN05.1. Significant positive values are observed in the northeast of the TRH region (lower elevation areas), while there is no increase along the southern border of the TRH region. The maximal increase of spring precipitation mainly occurs in the eastern TRH region (more than  $0.5 \text{ mm day}^{-1}$ ) and the northern part. In contrast, the pattern in ERA5 only shows some resemblance to the observation in the very southeast corner of the domain and indicates that the increase of spring precipitation in ERA5 mainly occurred in the southeastern and western TRH regions ([Fig. 7b](#)). ERA5 overestimates the observed increase of the spring precipitation in the western TRH region, whereas it underestimates it in the north. The overestimation may be due to the high terrain in the western TRH region (above 5000 m; see [Figs. 1](#) and [3](#)), which is not properly resolved in the reanalysis. The spatial pattern of difference between the dry and wet periods based on ERA5 excluding the year 2009 is further examined and the result is similar to before ([Fig. S2](#)), which indicates that the wetting trend in ERA5 is not entirely defined by only one year but wetting is recurrent in the recent decade. The above results indicate that although ERA5 captures the wetting trend in the current decade, it cannot correctly capture the spatial pattern of the observed spring precipitation change. WRF also does not perform well in reproducing the pattern of the precipitation change. The pattern of WRFD01 is similar to WRFD02, which indicates that the higher resolution of the WRF model benefits only from the reduction of the precipitation wet bias but does not change the pattern of difference between the dry and wet periods ([Figs. 7c,d](#) and [6c](#)).

The pattern of the WRF model along the east of the TRH region looks good, but there is another large area with increments around  $94^\circ\text{E}$ , north of the southern border, where high mountains should have blocked or diminished any extra advection in wet years. The increments in the north of the southern border may be related to the poor representation of the moisture flux because of the complex terrain in the model ([Fig. 3](#)). The spatial pattern of WRFD02 is similar to WRFD01, while the wet bias of WRFD02 is reduced significantly. Therefore, the results of WRFD02 are used for the water budget analysis and comparison with ERA5 in the following.

#### b. Moisture budget for spring precipitation change

[Figure 8](#) shows the moisture transport and moisture convergence during the dry and wet periods based on ERA5 and WRF. ERA5 and WRF show similar results for the pattern of moisture fluxes. They both show two moisture transport pathways toward the TRH region: southwesterly moisture transport along the south edge of the TP across the southern boundary and the midlatitude westerlies moisture transport across the western boundary ([Simmonds et al. 1999](#); [Shang et al. 2021](#)). The westerly moisture fluxes prevail over the TRH region. The positive moisture convergence over the TRH region is sustained by the westerly and southerly inflow across the western and southern boundaries, which exceeded the eastward outflow across the eastern boundary. It should be noted that the moisture convergence here is the average across a lot of noise. ERA5 and WRF both display intense moisture convergence over the southern region of the eastern Himalayas due to the blocking of the southerly water vapor by the high terrain. The difference is that the WRF Model shows strong moisture divergence along the Himalayas whereas this is not obvious in ERA5.

To understand the individual components of the atmospheric moisture budget governing the spring precipitation change over the TRH region, [Fig. 9](#) shows the spatial patterns for the differences of evapotranspiration, moisture convergence, and the residual between the wet period and the dry period based on

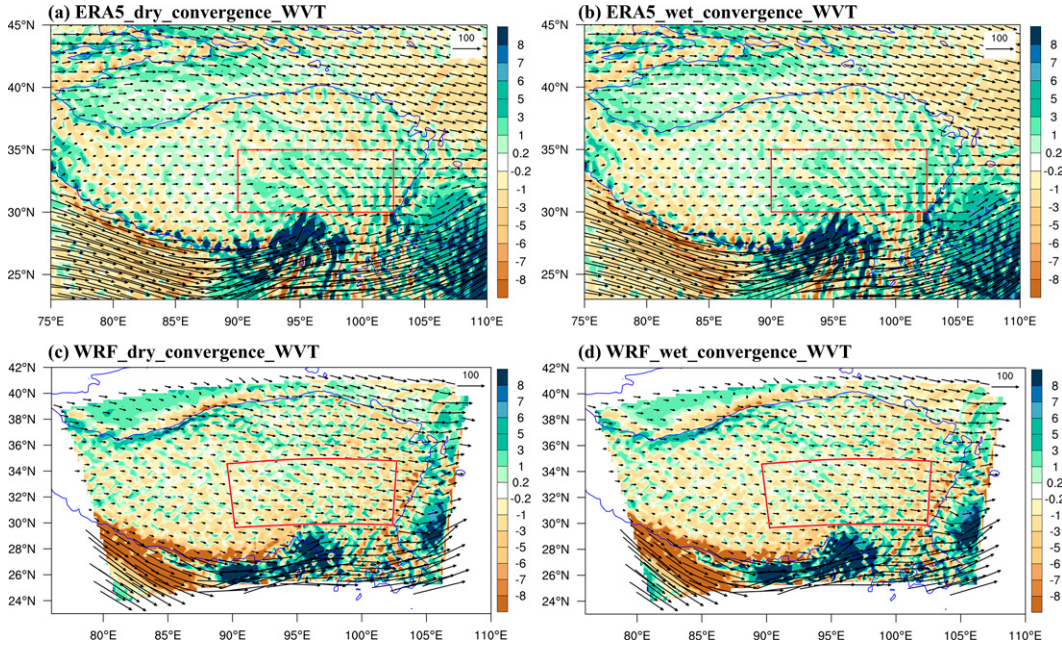


FIG. 8. Spring integrated moisture transport (vectors;  $\text{kg m}^{-1} \text{s}^{-1}$ ) and moisture convergence (color;  $\text{mm day}^{-1}$ ) based on (a),(b) ERA5 and (c),(d) WRF during (left) the dry period and (right) the wet period. The red rectangle denotes the location of our study region (D02).

ERA5 and WRF, respectively. The results for ERA5 show a large increase of evapotranspiration in the area around  $96^{\circ}\text{--}98^{\circ}\text{E}$  and  $31^{\circ}\text{--}32^{\circ}\text{N}$  (Fig. 9a). The WRF simulations show an increase of evapotranspiration in the eastern TRH region

(east of  $98^{\circ}\text{E}$ ) and almost no change in other areas. For the difference of moisture convergence (Figs. 9b,c), the ERA5 and the WRF Model both show a similar spatial pattern to their pattern of precipitation change (Figs. 7b,d). The differences of the

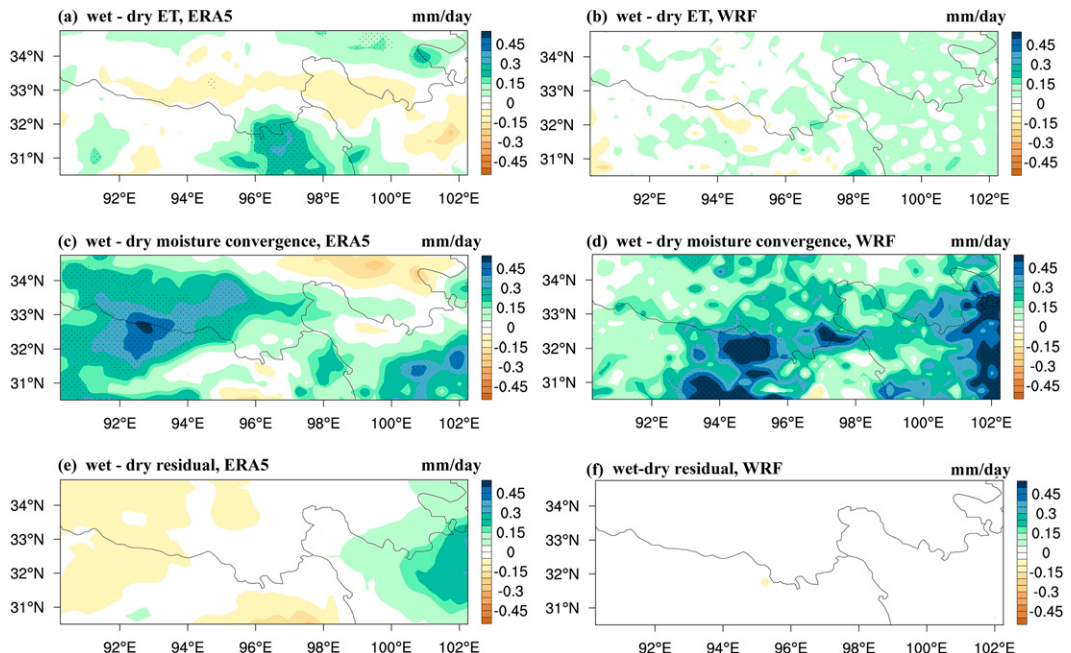


FIG. 9. Spatial pattern of the differences of individual atmospheric water budget items in spring corresponding to the change of precipitation between the wet period (2009–18) and the dry period (1979–88) based on (a),(c),(e) ERA5 and (b),(d),(f) WRF. Dotted regions indicate that differences are statistically significant at the 95% confidence level.

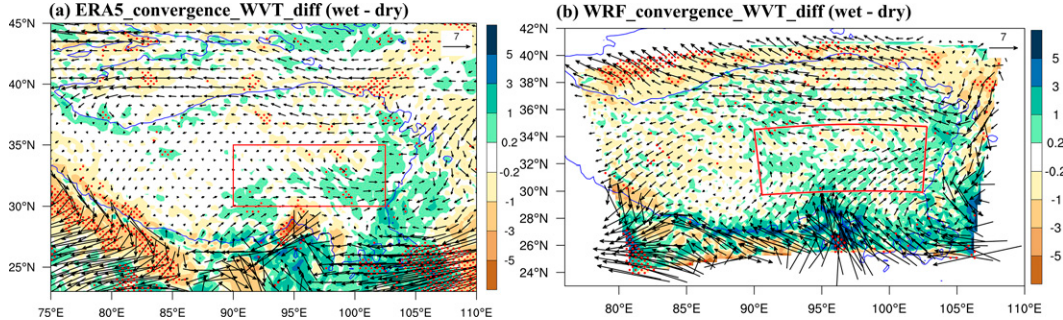


FIG. 10. Differences of the spring integrated moisture transport (vectors;  $\text{kg m}^{-1} \text{s}^{-1}$ ) and moisture convergence (color;  $\text{mm day}^{-1}$ ) between the wet period and the dry period based on (a) ERA5 and (b) WRF. Dotted regions indicate differences are statistically significant at the 95% confidence level.

residual from ERA5 show positive values in the eastern TRH region and small negative values in the northwestern TRH region (Fig. 9e), which may be related to numerical uncertainties in the budget evaluation method from ERA5 (Dee et al. 2011). The differences of the residual from WRF are very small (close to 0) across the entire study region, which demonstrates the advantage of the online calculation of the atmospheric water budget. In general, the spatial change of the moisture convergence dominates the change of spring precipitation over the TRH region.

The difference of the integrated moisture transport between the wet and dry periods based on ERA5 (Fig. 10a) indicates that the westerly moisture transport enhanced over the TRH region, resulting in the strengthened moisture convergence in the eastern region of the study region. The WRF Model shows an intense enhancement of the southerly moisture transport

across the southern boundary and an enhancement of westerlies over the TRH region during the wet period, leading to enhanced moisture convergence in the eastern region (Fig. 9d). Compared to ERA5, the enhancement of the southerly water fluxes described by WRF is stronger.

To assess the dynamic and thermodynamic contributions to the change of the moisture convergence and fluxes, the decomposition results of the moisture convergence based on ERA5 and WRF are shown in Fig. 11. The dynamic component of the moisture convergence based on ERA5 and WRF both display a similar spatial pattern to their patterns of moisture convergence differences between the wet period and the dry period (Figs. 9c and 8d). The dynamic water fluxes display easterly anomalies in the TP, implying the weakened westerlies in the recent decade. The easterly anomalies over the TRH region are favorable for convergence in this region (Sun et al. 2020;

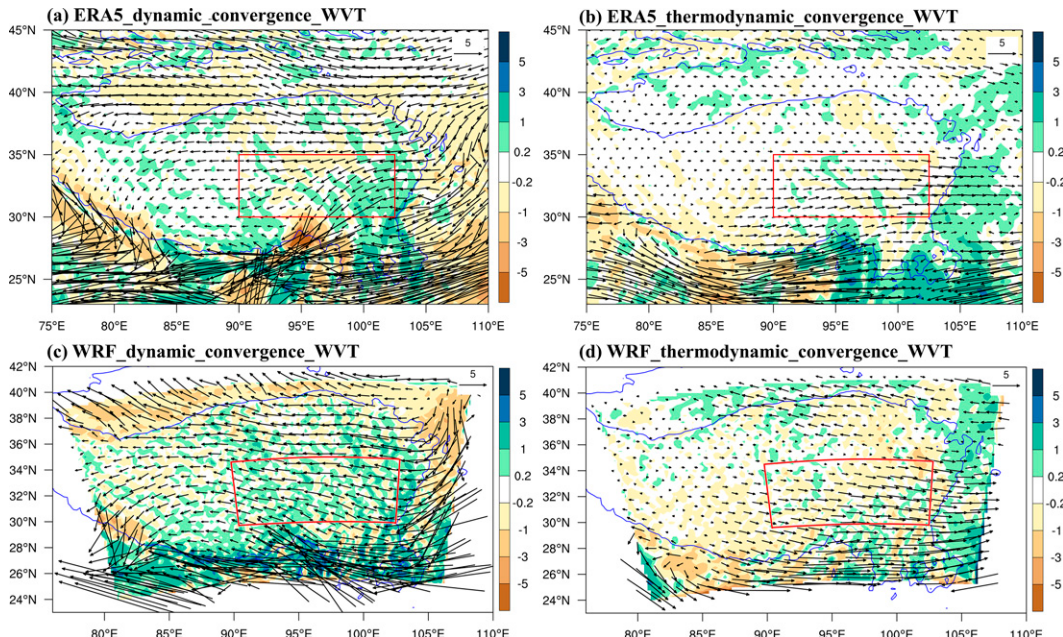


FIG. 11. The moisture convergence (color;  $\text{mm day}^{-1}$ ) and integrated moisture transport (vectors;  $\text{kg m}^{-1} \text{s}^{-1}$ ) contributed by (a),(c) the dynamic term related to the change of winds and (b),(d) the thermodynamic term related to the change of the specific humidity based on (top) ERA5 and (bottom) WRF.

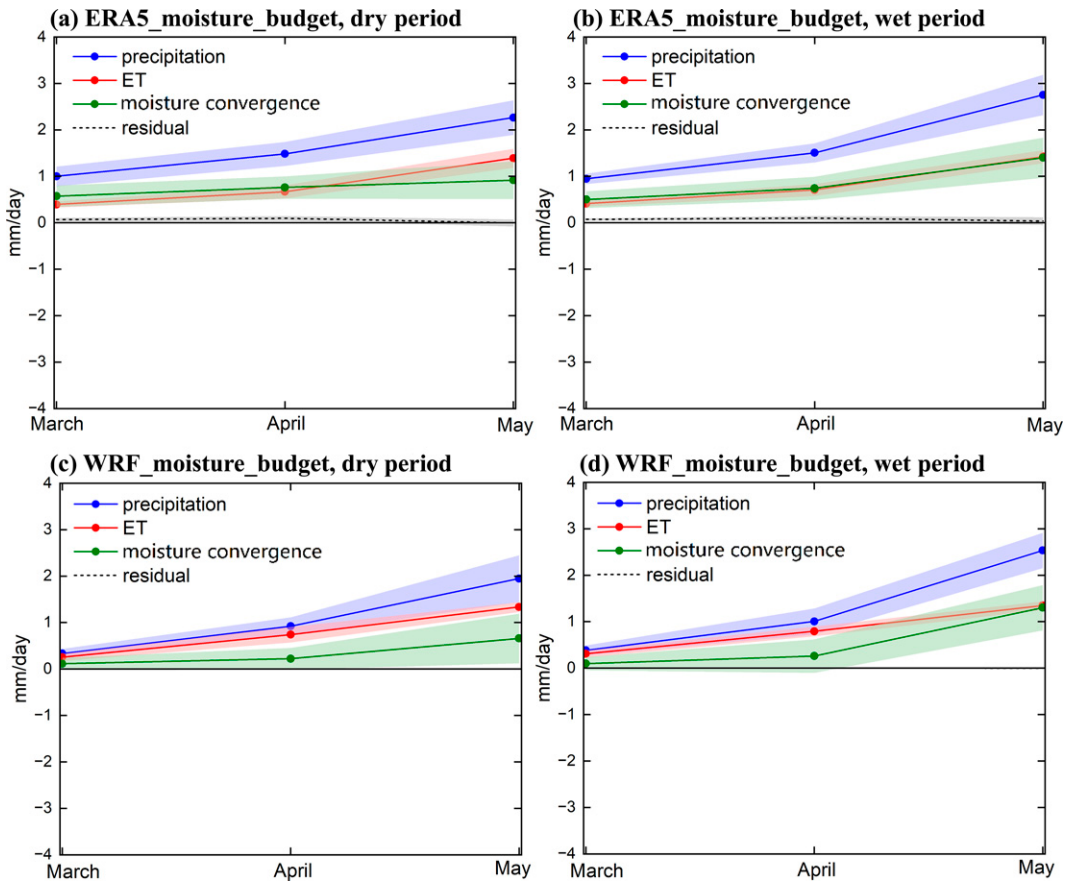


FIG. 12. Mean monthly precipitation, evapotranspiration, net moisture transport, and the residual during the dry and wet periods based on (a),(b) ERA5 and (c),(d) WRF. The shadows indicate the standard deviation of the mean value.

(Zhou et al. 2019; Lin et al. 2013; Shang et al. 2021). Compared to the dynamic term, the changes in the magnitude of the thermodynamic term are smaller. The thermodynamic terms based on ERA5 and WRF both show moisture divergence in the TP. But the thermodynamic water fluxes reveal enhanced westerly moisture transport, which implies the enhancement of the specific humidity in the TP. In conclusion, the decomposition results based on ERA5 and WRF indicate that the enhanced moisture inflow is sustained by enhanced mass flux (dynamic component), and the enhanced moisture outflow is sustained by increased moisture (thermodynamic component).

Figure 12 shows the individual mean monthly atmospheric water budget components (precipitation, evapotranspiration, moisture convergence, residual) during the dry and wet periods from ERA5 and WRF. Both ERA5 and WRF show the largest evapotranspiration, net atmospheric water transport, and precipitation in May. The monthly budget from ERA5 shows a similar magnitude for the moisture convergence and the evapotranspiration over the TRH region, whereas the WRF budget suggests that the total evapotranspiration is much larger. The atmospheric moisture convergence is additionally calculated with the input/output of the water fluxes across the lateral boundaries (the four boundaries of our studied rectangle region). For the TRH region, the

moisture inflow is mainly from the southern and western boundaries, and the fluxes from the north only play a minor role. The moisture outflow predominates at the eastern boundary (Figs. S3 and S4). For May, the moisture inflow from the southern direction dominates, both for the wet and dry periods. This month corresponds to the onset of the South Asian monsoon.

Figures 13a and 13b further show the differences of the monthly individual atmospheric water budget components between the wet and dry periods from ERA5 and WRF, respectively. The ERA5 and the WRF Model show similar results, which display the highest increase of moisture convergence in May, while there is almost no change for evapotranspiration in the whole spring. Figures 13c and 13d show the differences of the monthly water fluxes across four lateral boundaries in our study region between the wet period and the dry period. The atmospheric water transport change mainly occurs in May with the onset of the South Asian summer monsoon bringing abundant atmospheric water. The ERA5 and WRF model both show enhanced water transport across the southern and western boundaries in May during the wet period, which is an increase in the main contribution of atmospheric water to the TRH region. Enhanced output from the eastern boundary in May is also found with both ERA5 and WRF.

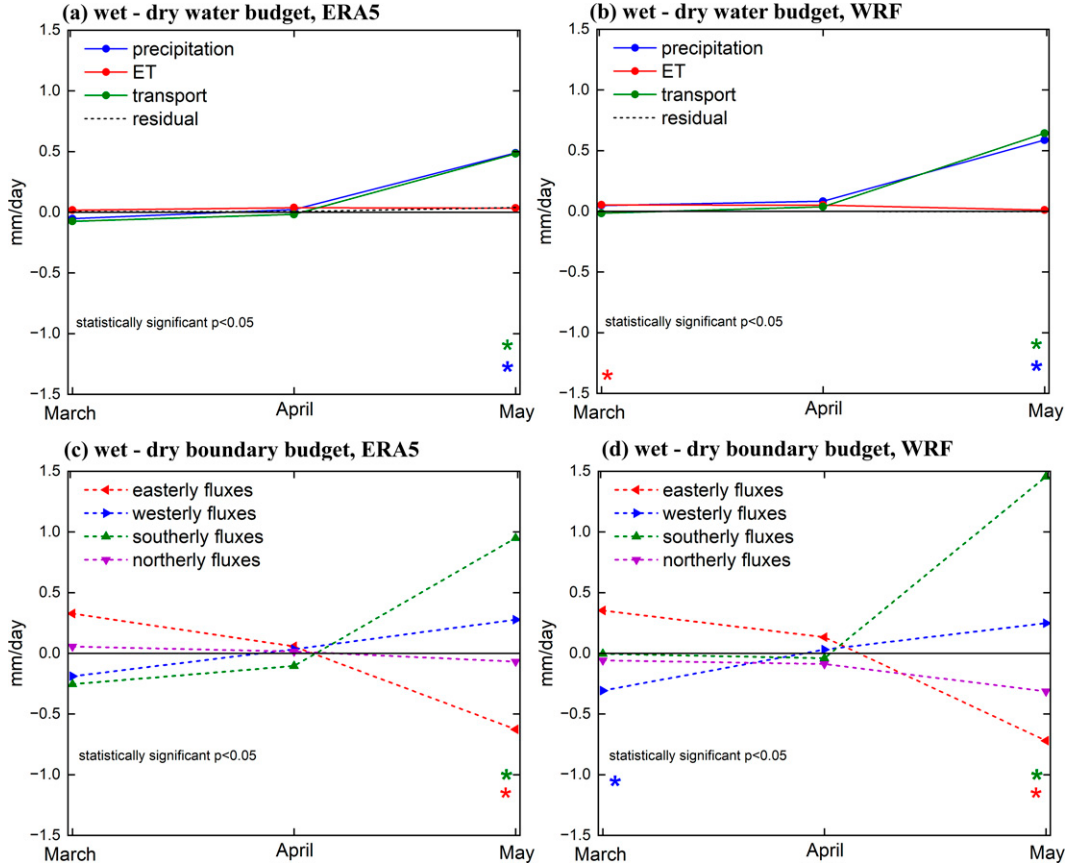


FIG. 13. Differences in monthly precipitation, evapotranspiration, net moisture transport, residual, and boundary water fluxes between the wet and dry periods based on (a),(c) ERA5 and (b),(d) WRF. The asterisks (\*) with different colors indicate that the differences of the respective variables between the dry period and the wet period in every month are statistically significant at the 95% confidence level.

The enhanced moisture output to the east can be interpreted as a consequence of the increased atmospheric water input from the western and southern boundaries. Nevertheless, the increase in moisture output across the eastern boundary is not as great as the increase in inflows at the western and southern boundaries. In general, this differential budget analysis shows that the enhancement of the spring precipitation observed in recent years over the TRH region is mainly because the enhanced southerly water fluxes across the southern boundary exceeded the enhanced moisture outflow across the eastern boundary. The enhanced moisture inflow is related to the easterly wind anomalies and enhanced southerly winds (Fig. 11). The easterly anomalies may be associated with an anticyclone to the north of the TRH region and the enhanced southerly moisture transport may be caused by the La Niña pattern in the Pacific (Sun and Wang 2018).

#### c. Spring atmospheric water budget differences between WRF and ERA5

Figures 14a and 14b show the differences in monthly precipitation, evapotranspiration, moisture transport, and the residual between WRF and ERA5 during the wet and dry periods

separately. In agreement with previous results, the WRF model simulates less precipitation than ERA5, associated with a reduced wet bias relative to observations (Figs. 2 and 4). The lesser precipitation in WRF compared to ERA5 is due to the weaker simulated moisture convergence (Figs. 14a,b), which is evidence of the potential of high-resolution modeling for evaluating climate change in this unique domain (Fig. 3; Zhou et al. 2021). The evapotranspiration simulated from WRF remains close to that from ERA5. Figures 14c and 14d, as well as Fig. S3c, show the differences of monthly and yearly atmospheric water fluxes through four lateral boundaries between WRF simulations and the ERA5 data during the dry and wet periods separately. Both during the dry and wet periods, the WRF model simulates more atmospheric water input from the northern boundary in the whole spring and more moisture output from the eastern boundary in May compared to the ERA5 data. Meanwhile, less southerly water fluxes are found with WRF both in the dry and wet periods (Figs. 14c,d; see also Fig. S3c). Thus, the reduced spring precipitation in WRF compared to ERA5 is due to a weaker simulated southerly water flux entering the TRH region, which is assumed to be a consequence of the higher resolution and a better representation of orographic barrier effects in the Himalayan region (Fig. 3; Bhatt and Nakamura 2005).

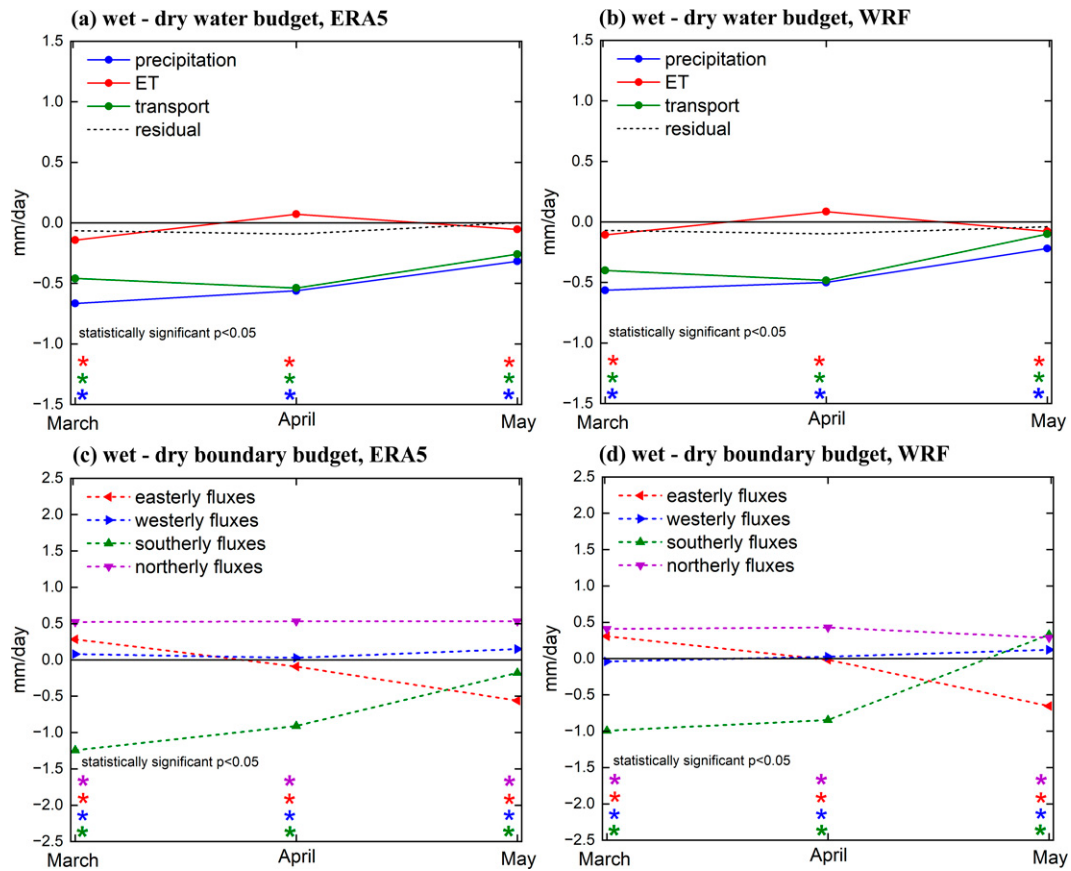


FIG. 14. Differences in monthly precipitation, evapotranspiration, net moisture transport, residual, and boundary water fluxes between (left) ERA5 and (right) WRF during (a),(c) the dry period and (b),(d) the wet period. The asterisks (\*) with different colors indicate that the differences of the respective variables between the dry period and the wet period in every month are statistically significant at the 95% confidence level.

#### d. Regional precipitation recycling differences between the wet period and the dry period

The evaluation of WRF results indicates that the setup of the WRF Model in this study is suitable for representing the variability of the land–atmosphere system in our study area. The ET-tagging method embedded in WRF allows us to quantify the contribution of regional land evapotranspiration to regional precipitation, which is usually measured with the precipitation recycling ratio. Figure 15 displays the spatial pattern of mean-tagged precipitation during the dry period, the wet period, and their corresponding difference (wet minus dry). The tagged precipitation is in the northeastern TRH region and decreases from northeast to southwest. This distribution of tagged precipitation is attributed to the prevailing westerly winds in the TP (Fig. 8; Ma et al. 2018; Dong et al. 2010; Yang et al. 2014; Shang et al. 2021) and is influenced by the topography (Figs. 1 and 3), resulting in the tagged precipitation falling in the eastern TP. The difference of tagged precipitation between the wet and dry periods shows that the tagged precipitation has increased largely in the eastern TRH region (Fig. 15c) related to the enhancement of evapotranspiration during the wet period (Fig. 9b). Figure 16 further

displays the spatial pattern of the spring precipitation recycling ratio during the dry and wet periods and their corresponding difference (wet minus dry). The precipitation recycling ratio displays a decrease from the northeast to the southwest, similar to the tagged precipitation during both the dry and wet periods. The mean precipitation recycling ratio averaged over the TRH region is about 12%. For comparison, Gao et al. (2020) obtained a regional precipitation recycling of 30% in spring for the TP region, which covers an area about 3 times larger than our TRH region. Such a scale effect is expected (Trenberth 1999; Arnault et al. 2016). The reasonable representation of evapotranspiration and precipitation in our simulations implies that our estimation reasonably captures the precipitation recycling process in this case study.

The area means precipitation recycling ratio decreased during the wet period (about 11.5% during the dry period and 10.7% during the wet period). The difference in precipitation recycling ratio between the wet and dry periods reveals that the recycling process is weakened over most of the TRH region in the recent wet years, although the total spring precipitation has increased. This indicates that the spring precipitation increase over the TRH region is mainly dominated by the external

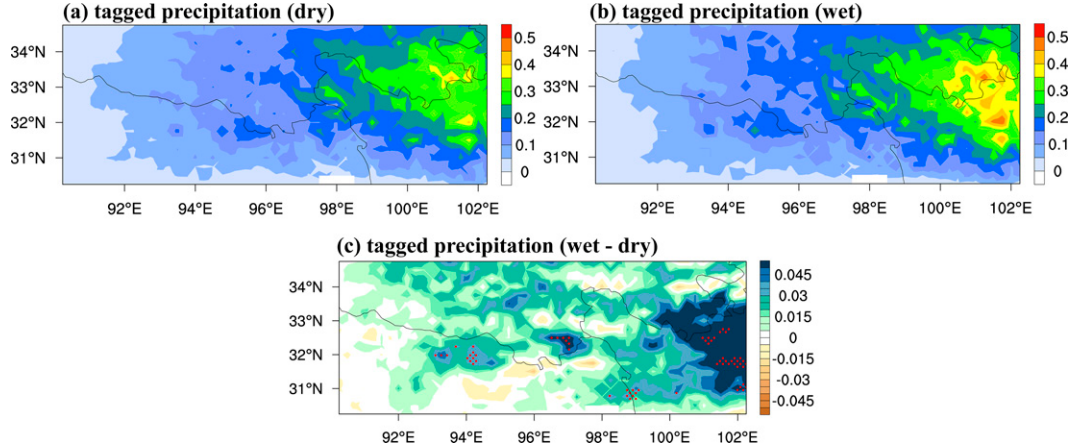


FIG. 15. Spatial pattern of the tagged precipitation during (a) the dry period and (b) the wet period, and (c) their corresponding differences ( $\text{mm day}^{-1}$ ). Dotted regions indicate that differences are statistically significant at the 95% confidence level.

atmospheric water transport related to the large-scale circulations. Accordingly, the large increase of spring precipitation produced by the external moisture decreases the relative contribution of evapotranspiration to precipitation in recent wet years, so the recycling process is more important during relatively dry years. Nevertheless, the contribution of the local evapotranspiration cannot be ignored as the tagged precipitation has increased during the wet period.

#### 4. Summary and conclusions

In this study, the characteristics of spring precipitation over the TRH region from 1979 to 2018 have been investigated based on the high-resolution daily China gridded dataset (CN05.1). The observational data showed that the spring precipitation in our study region increased significantly from the beginning of the 2000s. The global reanalysis ERA5 and the regional climate model WRF were further applied to investigate the atmospheric water budget related to the change of

the spring precipitation in this region. Therefore, two 10-yr subperiods (the relatively dry period from 1979 to 1988 and the relative wet period from 2009 to 2018) were simulated by WRF. For the temporal change of the spring precipitation, the ERA5 data captured the precipitation trend but with considerable overestimation (about  $0.6 \text{ mm day}^{-1}$ ). The WRF model performed better than ERA5 by decreasing the wet bias (the overestimation decreased from  $0.6$  to  $0.14 \text{ mm day}^{-1}$ ). For the spatial pattern of the spring precipitation change (wet period minus dry period) over the TRH region, ERA5 and WRF both do not perform well.

Both ERA5 and the WRF model indicated that the recent increase of spring precipitation over the TRH region is mostly related to a change of moisture convergence in May, while ET was barely changed. The decomposition of the moisture convergence and fluxes based on ERA5 and WRF both revealed that the dynamic component related to the change of horizontal winds dominates the enhanced moisture inflow, while the enhanced moisture outflow is sustained by the

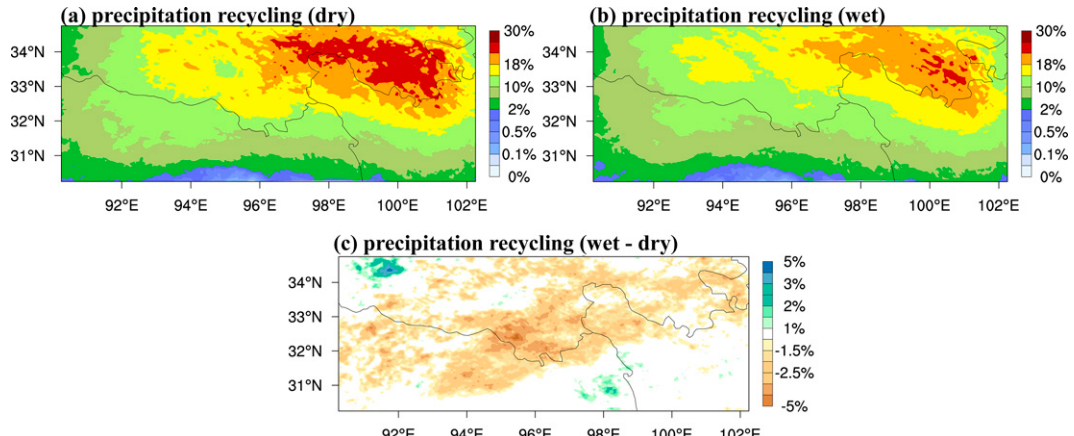


FIG. 16. Spatial pattern of the precipitation recycling ratio during (a) the dry period and (b) the wet period, and (c) their corresponding differences.

increased moisture (thermodynamic component). The net atmospheric moisture transport calculated by the input/output of the water vapor fluxes across the four lateral boundaries in our study region showed that the moisture inflow is mainly from the southern and western boundaries, and the outflow is from the eastern boundary. The change of atmospheric moisture transport between the wet and dry periods mainly occurred in May during the South Asian summer monsoon onset. The water fluxes across the southern boundary mostly contributed to the enhancement of the moisture convergence over the TRH region, as demonstrated by both ERA5 and the WRF model.

Regarding the comparison of the atmospheric water budget simulated by WRF and ERA5, the moisture convergence simulated by WRF was lower than that in ERA5. The reduced moisture convergence from WRF was related to a reduction of simulated water fluxes from the southern boundary compared to ERA5, leading to a reduction of the wet bias in WRF.

Based on the ET-tagging method embedded in the WRF model, the contribution of land evapotranspiration to regional precipitation (regional precipitation recycling) was further quantified. The result showed that spring precipitation from evapotranspiration was mainly distributed in the northeastern TRH region because of the prevailing westerly winds in the TP. The precipitation recycling ratio decreased in the recent wet period, as the recent increase of spring precipitation over the TRH region was mainly dominated by external moisture transport. But the contribution of the local evapotranspiration should not be ignored as the tagged precipitation increased during the wet period.

It is concluded that the ERA5 reanalysis data overestimated the moisture convergence and precipitation in spring due to the influence of the complex terrain, which is not properly represented in the reanalysis. The comparison of the atmospheric water budget from ERA5 and WRF evidenced that the dynamical downscaling offers a sophisticated method for refining and improving the description of the regional atmospheric water budget in the unique high mountainous region. Nevertheless, ERA5 is still suitable for large-scale analysis of long-term climate change research because of the expensive computation for the downscaling model. The downscaling model can provide a more accurate estimate of regional-scale climate change, such as land–atmosphere interactions. In the future, the model can be used to assess the potential impacts of other factors on precipitation change over the TRH region, such as the land-use change, including lake expansion and permafrost degradation due to global warming. Further studies should also be conducted to couple the “tagging method” with comprehensive land surface schemes to enhance the understanding of the land–atmosphere interaction.

**Acknowledgments.** This research is funded by the National Natural Science Foundation of China (41871078, 42171019) and the Chinese Scholarship Council. Joël Arnault and Jianhui Wei are supported by the German Research Foundation grants (DFG, AccHydro KU 2090/11-1 and AR 1183/2-1). Zhenyu

Zhang is supported by the German Federal Ministry of Science and Education (BMBF) project (SALDi, 01LL1701B). We also acknowledge the kind support by the Supercomputing Center of Lanzhou University and the High-Performance Computer in KIT/IMK-IFU. We thank the editor and three anonymous reviewers for their helpful comments.

**Data availability statement.** The CN05.1 data are obtained from the China Meteorology Administration’s National Climate Center. The ERA5 reanalysis is downloaded from <https://cds.climate.copernicus.eu/cdsapp#!/dataset/reanalysis-era5-pressure-levels?tab=overview>. The GLEAM 3.5a dataset is available at <https://www.gleam.eu/>.

## REFERENCES

- Arnault, J., R. Knoche, J. Wei, and H. Kunstmann, 2016: Evaporation tagging and atmospheric water budget analysis with WRF: A regional precipitation recycling study for West Africa. *Water Resour. Res.*, **52**, 1544–1567, <https://doi.org/10.1002/2015WR017704>.
- , J. Wei, T. Rummel, B. Fersch, Z. Zhang, G. Jung, S. Wagner, and H. Kunstmann, 2019: A joint soil–vegetation–atmospheric water tagging procedure with WRF-Hydro: Implementation and application to the case of precipitation partitioning in the upper Danube River basin. *Water Resour. Res.*, **55**, 6217–6243, <https://doi.org/10.1029/2019WR024780>.
- , and Coauthors, 2021: Lateral terrestrial water flow contribution to summer precipitation at continental scale—A comparison between Europe and West Africa with WRF-Hydro-tag ensembles. *Hydrol. Processes*, **35**, e14183, <https://doi.org/10.1002/hyp.14183>.
- Beljaars, A. C. M., A. R. Brown, and N. Wood, 2004: A new parametrization of turbulent orographic form drag. *Quart. J. Roy. Meteor. Soc.*, **130**, 1327–1347, <https://doi.org/10.1256/qj.03.73>.
- Bhatt, B. C., and K. Nakamura, 2005: Characteristics of monsoon rainfall around the Himalayas revealed by TRMM Precipitation Radar. *Mon. Wea. Rev.*, **133**, 149–165, <https://doi.org/10.1175/MWR-2846.1>.
- Brown, P. J., and C. D. Kummerow, 2014: An assessment of atmospheric water budget components over tropical oceans. *J. Climate*, **27**, 2054–2071, <https://doi.org/10.1175/JCLI-D-13-00385.1>.
- Brubaker, K. L., D. Entekhabi, and P. S. Eagleson, 1993: Estimation of continental precipitation recycling. *J. Climate*, **6**, 1077–1089, [https://doi.org/10.1175/1520-0442\(1993\)006<1077:EOCPR>2.0.CO;2](https://doi.org/10.1175/1520-0442(1993)006<1077:EOCPR>2.0.CO;2).
- Burde, G. I., and A. Zangvil, 2001: The estimation of regional precipitation recycling. Part II: A new recycling model. *J. Climate*, **14**, 2509–2527, [https://doi.org/10.1175/1520-0442\(2001\)014<2509:TEOPR>2.0.CO;2](https://doi.org/10.1175/1520-0442(2001)014<2509:TEOPR>2.0.CO;2).
- Castro, C. L., R. A. Pielke, and G. Leoncini, 2005: Dynamical downscaling: Assessment of value retained and added using the Regional Atmospheric Modeling System (RAMS). *J. Geophys. Res.*, **110**, D05108, <https://doi.org/10.1029/2004JD004721>.
- Collier, E., T. Mölg, F. Maussion, D. Scherer, C. Mayer, and A. B. G. Bush, 2013: High-resolution interactive modelling of the mountain glacier–atmosphere interface: An application over the Karakoram. *Cryosphere*, **7**, 779–795, <https://doi.org/10.5194/tc-7-779-2013>.

- Cullather, R. I., D. H. Bromwich, and M. C. Serreze, 2000: The atmospheric hydrologic cycle over the Arctic basin from reanalyses. Part I: Comparison with observations and previous studies. *J. Climate*, **13**, 923–937, [https://doi.org/10.1175/1520-0442\(2000\)013<0923:TAHCOT>2.0.CO;2](https://doi.org/10.1175/1520-0442(2000)013<0923:TAHCOT>2.0.CO;2).
- Dee, D. P., and Coauthors, 2011: The ERA-Interim reanalysis: Configuration and performance of the data assimilation system. *Quart. J. Roy. Meteor. Soc.*, **137**, 553–597, <https://doi.org/10.1002/qj.828>.
- de Oliveira, V. A., C. R. de Mello, M. R. Viola, and R. Srinivasan, 2017: Assessment of climate change impacts on streamflow and hydropower potential in the headwater region of the Grande river basin, southeastern Brazil. *Int. J. Climatol.*, **37**, 5005–5023, <https://doi.org/10.1002/joc.5138>.
- Dominguez, F., G. Miguez-Macho, and H. Hu, 2016: WRF with water vapor tracers: A study of moisture sources for the North American monsoon. *J. Hydrometeor.*, **17**, 1915–1927, <https://doi.org/10.1175/JHM-D-15-0221.1>.
- Dong, H., H. Jiang, B. Yu, and X. Liu, 2010: Impacts of environmental change and human activity on microbial ecosystems on the Tibetan Plateau, NW China. *Geol. Soc. Amer. Today*, **20**, 4–10, <https://doi.org/10.1130/GSATG75A.1>.
- Dudhia, J., 1989: Numerical study of convection observed during the winter monsoon experiment using a mesoscale two-dimensional model. *J. Atmos. Sci.*, **46**, 3077–3107, [https://doi.org/10.1175/1520-0469\(1989\)046<3077:NSOCOD>2.0.CO;2](https://doi.org/10.1175/1520-0469(1989)046<3077:NSOCOD>2.0.CO;2).
- Gao, Y., L. Cuo, and Y. Zhang, 2014: Changes in moisture flux over the Tibetan Plateau during 1979–2011 and possible mechanisms. *J. Climate*, **27**, 1876–1893, <https://doi.org/10.1175/JCLI-D-13-00321.1>.
- , J. Xu, and D. Chen, 2015: Evaluation of WRF mesoscale climate simulations over the Tibetan Plateau during 1979–2011. *J. Climate*, **28**, 2823–2841, <https://doi.org/10.1175/JCLI-D-14-00300.1>.
- , L. Xiao, D. Chen, J. Xu, and H. Zhang, 2018: Comparison between past and future extreme precipitations simulated by global and regional climate models over the Tibetan Plateau. *Int. J. Climatol.*, **38**, 1285–1297, <https://doi.org/10.1002/joc.5243>.
- , F. Chen, G. Miguez-Macho, and X. Li, 2020: Understanding precipitation recycling over the Tibetan Plateau using tracer analysis with WRF. *Climate Dyn.*, **55**, 2921–2937, <https://doi.org/10.1007/s00382-020-05426-9>.
- Hagemann, S., K. Arpe, and L. Bengtsson, 2005: Validation of the hydrological cycle of ERA-40. ERA-40 Rep. Series 24, 42 pp., <https://www.ecmwf.int/node/9728>.
- Hersbach, H., and Coauthors, 2018: Operational global reanalysis: progress, future directions and synergies with NWP. ERA Rep. Series 27, 65 pp., <https://doi.org/10.21957/tkic6g3wm>.
- Hong, S.-Y., Y. Noh, and J. Dudhia, 2006: A new vertical diffusion package with an explicit treatment of entrainment processes. *Mon. Wea. Rev.*, **134**, 2318–2341, <https://doi.org/10.1175/MWR3199.1>.
- Immerzeel, W. W., L. P. H. Van Beek, and M. F. P. Bierkens, 2010: Climate change will affect the Asian water towers. *Science*, **328**, 1382–1385, <https://doi.org/10.1126/science.1183188>.
- Insua-Costa, D., and G. Miguez-Macho, 2018: A new moisture tagging capability in the Weather Research and Forecasting model: Formulation, validation and application to the 2014 Great Lake-effect snowstorm. *Earth Syst. Dyn.*, **9**, 167–185, <https://doi.org/10.5194/esd-9-167-2018>.
- Ji, P., X. Yuan, F. Ma, and M. Pan, 2020: Accelerated hydrological cycle over the Sanjiangyuan region induces more streamflow extremes at different global warming levels. *Hydrol. Earth Syst. Sci.*, **24**, 5439–5451, <https://doi.org/10.5194/hess-24-5439-2020>.
- Ji, Z., and S. Kang, 2013: Double-nested dynamical downscaling experiments over the Tibetan Plateau and their projection of climate change under two RCP scenarios. *J. Atmos. Sci.*, **70**, 1278–1290, <https://doi.org/10.1175/JAS-D-12-0155.1>.
- Jiang, C., and L. Zhang, 2016: Effect of ecological restoration and climate change on ecosystems: A case study in the Three-Rivers Headwater Region, China. *Environ. Monit. Assess.*, **188**, 382, <https://doi.org/10.1007/s10661-016-5368-2>.
- , D. Li, Y. Gao, W. Liu, and L. Zhang, 2017: Impact of climate variability and anthropogenic activity on streamflow in the Three Rivers Headwater Region, Tibetan Plateau, China. *Theor. Appl. Climatol.*, **129**, 667–681, <https://doi.org/10.1007/s00704-016-1833-7>.
- Kain, J. S., and J. M. Fritsch, 1992: The role of the convective “trigger function” in numerical forecasts of mesoscale convective systems. *Meteor. Atmos. Phys.*, **49**, 93–106, <https://doi.org/10.1007/BF01025402>.
- Kalnay, E., and Coauthors, 1996: The NCEP/NCAR 40-Year Reanalysis Project. *Bull. Amer. Meteor. Soc.*, **77**, 437–471, [https://doi.org/10.1175/1520-0477\(1996\)077<0437:TNYRP>2.0.CO;2](https://doi.org/10.1175/1520-0477(1996)077<0437:TNYRP>2.0.CO;2).
- Karki, R., S. ul Hasson, L. Gerlitz, U. Schickhoff, T. Scholten, and J. Böhner, 2017: Quantifying the added value of convection-permitting climate simulations in complex terrain: A systematic evaluation of WRF over the Himalayas. *Earth Syst. Dyn.*, **8**, 507–528, <https://doi.org/10.5194/esd-8-507-2017>.
- Knoche, H. R., and H. Kunstmann, 2013: Tracking atmospheric water pathways by direct evaporation tagging: A case study for West Africa. *J. Geophys. Res. Atmos.*, **118**, 12 345–12 358, <https://doi.org/10.1002/2013JD019976>.
- Li, L., W. Li, and A. P. Barros, 2013: Atmospheric moisture budget and its regulation of the summer precipitation variability over the southeastern United States. *Climate Dyn.*, **41**, 613–631, <https://doi.org/10.1007/s00382-013-1697-9>.
- Li, X., G. Brieler, D. Shi, Y. Xie, and H. Sun, 2012: Ecological protection and restoration in Sanjiangyuan National Nature Reserve, Qinghai province, China. *Perspectives on Environmental Management and Technology in Asian River Basins*, D. Higgitt, Ed., Springer, 93–120.
- Li, Z., and Coauthors, 2021: Hydrological effects of multiphase water transformation in Three-River headwaters region, China. *J. Hydrol.*, **601**, 126662, <https://doi.org/10.1016/j.jhydrol.2021.126662>.
- Lin, C., K. Yang, J. Qin, and R. Fu, 2013: Observed coherent trends of surface and upper-air wind speed over China since 1960. *J. Climate*, **26**, 2891–2903, <https://doi.org/10.1175/JCLI-D-12-00093.1>.
- Liu, T., P. Willems, X. L. Pan, A. M. Bao, X. Chen, F. Veroustraete, and Q. H. Dong, 2011: Climate change impact on water resource extremes in a headwater region of the Tarim basin in China. *Hydrol. Earth Syst. Sci.*, **15**, 3511–3527, <https://doi.org/10.5194/hess-15-3511-2011>.
- Liu, X., and B. Chen, 2000: Climatic warming in the Tibetan Plateau during recent decades. *Int. J. Climatol.*, **20**, 1729–1742, [https://doi.org/10.1002/1097-0088\(20001130\)20:14<1729::AID-JOC556>3.0.CO;2-Y](https://doi.org/10.1002/1097-0088(20001130)20:14<1729::AID-JOC556>3.0.CO;2-Y).
- , Z. Cheng, L. Yan, and Z. Y. Yin, 2009: Elevation dependency of recent and future minimum surface air temperature trends in the Tibetan Plateau and its surroundings. *Global Planet. Change*, **68**, 164–174, <https://doi.org/10.1016/j.gloplacha.2009.03.017>.

- Ma, Y., M. Lu, H. Chen, M. Pan, and Y. Hong, 2018: Atmospheric moisture transport versus precipitation across the Tibetan Plateau: A mini-review and current challenges. *Atmos. Res.*, **209**, 50–58, <https://doi.org/10.1016/j.atmosres.2018.03.015>.
- Martens, B., and Coauthors, 2017: GLEAM v3: Satellite-based land evaporation and root-zone soil moisture. *Geosci. Model Dev.*, **10**, 1903–1925, <https://doi.org/10.5194/gmd-10-1903-2017>.
- Miralles, D. G., T. R. H. Holmes, R. A. M. De Jeu, J. H. Gash, A. G. C. A. Meesters, and A. J. Dolman, 2011: Global land-surface evaporation estimated from satellite-based observations. *Hydrol. Earth Syst. Sci.*, **15**, 453–469, <https://doi.org/10.5194/hess-15-453-2011>.
- Mlawer, E. J., S. J. Taubman, P. D. Brown, M. J. Iacono, and S. A. Clough, 1997: Radiative transfer for inhomogeneous atmospheres: RRTM, a validated correlated- $k$  model for the longwave. *J. Geophys. Res.*, **102**, 16 663–16 682, <https://doi.org/10.1029/97JD00237>.
- Mughal, M. O., M. Lynch, F. Yu, B. McGann, F. Jeanneret, and J. Sutton, 2017: Wind modelling, validation and sensitivity study using Weather Research and Forecasting model in complex terrain. *Environ. Modell. Software*, **90**, 107–125, <https://doi.org/10.1016/j.envsoft.2017.01.009>.
- Niu, G. Y., and Coauthors, 2011: The community Noah land surface model with multiparameterization options (Noah-MP): 1. Model description and evaluation with local-scale measurements. *J. Geophys. Res.*, **116**, D12109, <https://doi.org/10.1029/2010JD015139>.
- Peixóto, J. P., and A. H. Oort, 1984: Physics of climate. *Rev. Mod. Phys.*, **56**, 365, <https://doi.org/10.1103/RevModPhys.56.365>.
- Qian, S., Y. Fu, and F. F. Pan, 2010: Climate change tendency and grassland vegetation response during the growth season in Three-River source region. *Sci. China Earth Sci.*, **53**, 1506–1512, <https://doi.org/10.1007/s11430-010-4064-2>.
- Qin, J., K. Yang, S. Liang, and X. Guo, 2009: The altitudinal dependence of recent rapid warming over the Tibetan Plateau. *Climatic Change*, **97**, 321, <https://doi.org/10.1007/s10584-009-9733-9>.
- Qiu, J., 2008: China: The third pole. *Nature*, **454**, 393–396, <https://doi.org/10.1038/454393a>.
- Schmitz, J. T., and S. L. Mullen, 1996: Water vapor transport associated with the summertime North American monsoon as depicted by ECMWF analyses. *J. Climate*, **9**, 1621–1634, [https://doi.org/10.1175/1520-0442\(1996\)009<1621:WVTAWT>2.0.CO;2](https://doi.org/10.1175/1520-0442(1996)009<1621:WVTAWT>2.0.CO;2).
- Seager, R., and N. Henderson, 2013: Diagnostic computation of moisture budgets in the ERA-interim reanalysis with reference to analysis of CMIP-archived atmospheric model data. *J. Climate*, **26**, 7876–7901, <https://doi.org/10.1175/JCLI-D-13-00018.1>.
- , N. Naik, and G. A. Vecchi, 2010: Thermodynamic and dynamic mechanisms for large-scale changes in the hydrological cycle in response to global warming. *J. Climate*, **23**, 4651–4668, <https://doi.org/10.1175/2010JCLI3655.1>.
- Shang, S., and Coauthors, 2021: Associated atmospheric mechanisms for the increased cold season precipitation over the Three-River headwaters region from the late 1980s. *J. Climate*, **34**, 8033–8046, <https://doi.org/10.1175/JCLI-D-21-0077.1>.
- Shao, Q., W. Cao, J. Fan, L. Huang, and X. Xu, 2017: Effects of an ecological conservation and restoration project in the Three-River source region, China. *J. Geogr. Sci.*, **27**, 183–204, <https://doi.org/10.1007/s11442-017-1371-y>.
- Shi, H., T. Li, J. Wei, W. Fu, and G. Wang, 2016: Spatial and temporal characteristics of precipitation over the Three-River Headwaters region during 1961–2014. *J. Hydrol. Reg. Stud.*, **6**, 52–65, <https://doi.org/10.1016/j.ejrh.2016.03.001>.
- Shi, Y., G. Wang, and X. Gao, 2018: Role of resolution in regional climate change projections over China. *Climate Dyn.*, **51**, 2375–2396, <https://doi.org/10.1007/s00382-017-4018-x>.
- Simmonds, I., D. Bi, and P. Hope, 1999: Atmospheric water vapor flux and its association with rainfall over China in summer. *J. Climate*, **12**, 1353–1367, [https://doi.org/10.1175/1520-0442\(1999\)012<1353:AWVFAI>2.0.CO;2](https://doi.org/10.1175/1520-0442(1999)012<1353:AWVFAI>2.0.CO;2).
- Skamarock, W. C., and J. B. Klemp, 2008: A time-split nonhydrostatic atmospheric model for weather research and forecasting applications. *J. Comput. Phys.*, **227**, 3465–3485, <https://doi.org/10.1016/j.jcp.2007.01.037>.
- , and Coauthors, 2008: A description of the Advanced Research WRF version 3. NCAR Tech. Note NCAR/TN-475+STR, 113 pp., <https://doi.org/10.5065/D68S4MVH>.
- Sodemann, H., H. Wernli, and C. Schwierz, 2009: Sources of water vapour contributing to the Elbe flood in August 2002—A tagging study in a mesoscale model. *Quart. J. Roy. Meteor. Soc.*, **135**, 205–223, <https://doi.org/10.1002/qj.374>.
- Sun, B., and H. Wang, 2018: Interannual variation of the spring and summer precipitation over the Three River source region in China and the associated regimes. *J. Climate*, **31**, 7441–7457, <https://doi.org/10.1175/JCLI-D-17-0680.1>.
- Sun, J., K. Yang, W. Guo, Y. Wang, J. He, and H. Lu, 2020: Why has the inner Tibetan Plateau become wetter since the mid-1990s? *J. Climate*, **33**, 8507–8522, <https://doi.org/10.1175/JCLI-D-19-0471.1>.
- Tong, K.-T., F. Su, D. Yang, L. Zhang, and Z. Hao, 2014: Tibetan Plateau precipitation as depicted by gauge observations, reanalyses and satellite retrievals. *Int. J. Climatol.*, **34**, 265–285, <https://doi.org/10.1002/joc.3682>.
- Trenberth, K. E., 1999: Atmospheric moisture recycling: Role of advection and local evaporation. *J. Climate*, **12**, 1368–1381, [https://doi.org/10.1175/1520-0442\(1999\)012<1368:AMRROA>2.0.CO;2](https://doi.org/10.1175/1520-0442(1999)012<1368:AMRROA>2.0.CO;2).
- , and C. J. Guillemot, 1995: Evaluation of the global atmospheric moisture budget as seen from analyses. *J. Climate*, **8**, 2255–2272, [https://doi.org/10.1175/1520-0442\(1995\)008<2255:EOTGAM>2.0.CO;2](https://doi.org/10.1175/1520-0442(1995)008<2255:EOTGAM>2.0.CO;2).
- , and —, 1998: Evaluation of the atmospheric moisture and hydrological cycle in the NCEP/NCAR reanalyses. *Climate Dyn.*, **14**, 213–231, <https://doi.org/10.1007/s003820050219>.
- , L. Smith, T. Qian, A. Dai, and J. Fasullo, 2007: Estimates of the global water budget and its annual cycle using observational and model data. *J. Hydrometeorol.*, **8**, 758–769, <https://doi.org/10.1175/JHM600.1>.
- Uppala, S. M., and Coauthors, 2005: The ERA-40 Re-Analysis. *Quart. J. Roy. Meteor. Soc.*, **131**, 2961–3012, <https://doi.org/10.1256/qj.04.176>.
- Wang, Y., and Coauthors, 2020: Synergy of orographic drag parameterization and high resolution greatly reduces biases of WRF-simulated precipitation in central Himalaya. *Climate Dyn.*, **54**, 1729–1740, <https://doi.org/10.1007/s00382-019-05080-w>.
- , R. Ma, and G. Zhu, 2022: Improved prediction of hydraulic conductivity with a soil water retention curve that accounts for both capillary and adsorption forces. *Water Resour. Res.*, **58**, e2021WR031297, <https://doi.org/10.1029/2021WR031297>.
- Wei, J., H. R. Knoche, and H. Kunstmann, 2015: Contribution of transpiration and evaporation to precipitation: An ET-tagging study for the Poyang Lake region in Southeast China. *J. Geophys. Res. Atmos.*, **120**, 6845–6864, <https://doi.org/10.1002/2014JD022975>.

- Wu, J., and X.-J. Gao, 2013: A gridded daily observation dataset over China region and comparison with the other datasets. *Chin. J. Geophys.*, **56**, 1102–1111, <https://doi.org/10.6038/cjg20130406>.
- Xi, Y., C. Miao, J. Wu, Q. Duan, X. Lei, and H. Li, 2018: Spatio-temporal changes in extreme temperature and precipitation events in the Three-Rivers headwater region, China. *J. Geophys. Res. Atmos.*, **123**, 5827–5844, <https://doi.org/10.1029/2017JD028226>.
- Xu, J., and Coauthors, 2018: On the role of horizontal resolution over the Tibetan Plateau in the REMO regional climate model. *Climate Dyn.*, **51**, 4525–4542, <https://doi.org/10.1007/s00382-018-4085-7>.
- Yan, H., J. Huang, Y. He, Y. Liu, T. Wang, and J. Li, 2020: Atmospheric water vapor budget and its long-term trend over the Tibetan Plateau. *J. Geophys. Res. Atmos.*, **125**, e2020JD033297, <https://doi.org/10.1029/2020JD033297>.
- Yang, K., H. Wu, J. Qin, C. Lin, W. Tang, and Y. Chen, 2014: Recent climate changes over the Tibetan Plateau and their impacts on energy and water cycle: A review. *Global Planet. Change*, **112**, 79–91, <https://doi.org/10.1016/j.gloplacha.2013.12.001>.
- Yang, Z., and F. Dominguez, 2019: Investigating land surface effects on the moisture transport over South America with a moisture tagging model. *J. Climate*, **32**, 6627–6644, <https://doi.org/10.1175/JCLI-D-18-0700.1>.
- Yi, X., G. Li, and Y. Yin, 2013: Spatio-temporal variation of precipitation in the Three-River Headwater Region from 1961 to 2010. *J. Geogr. Sci.*, **23**, 447–464, <https://doi.org/10.1007/s11442-013-1021-y>.
- You, Q., K. Fraedrich, G. Ren, B. Ye, X. Meng, and S. Kang, 2012: Inconsistencies of precipitation in the eastern and central Tibetan Plateau between surface adjusted data and reanalysis. *Theor. Appl. Climatol.*, **109**, 485–496, <https://doi.org/10.1007/s00704-012-0594-1>.
- Zhang, W., T. Zhou, and L. Zhang, 2017: Wetting and greening Tibetan Plateau in early summer in recent decades. *J. Geophys. Res. Atmos.*, **122**, 5808–5822, <https://doi.org/10.1002/2017JD026468>.
- Zhang, Y., S. Zhang, X. Zhai, and J. Xia, 2012: Runoff variation and its response to climate change in the Three Rivers source region. *J. Geogr. Sci.*, **22**, 781–794, <https://doi.org/10.1007/s11442-012-0963-9>.
- , —, J. Fan, W. Cao, and H.-Y. Zhang, 2017: Spatial and temporal dynamics of grassland yield and its response to precipitation in the Three River Headwater Region from 2006 to 2013. *Acta Prataculturae Sin.*, **26**, 10–19, <http://cyxb.magtech.com.cn/EN/10.11686/cyxb2017008>.
- Zhang, Z., J. Arnault, S. Wagner, P. Laux, and H. Kunstmann, 2019: Impact of lateral terrestrial water flow on land-atmosphere interactions in the Heihe River basin in China: Fully coupled modeling and precipitation recycling analysis. *J. Geophys. Res. Atmos.*, **124**, 8401–8423, <https://doi.org/10.1029/2018JD030174>.
- , —, P. Laux, N. Ma, J. Wei, S. Shang, and H. Kunstmann, 2022: Convection-permitting fully coupled WRF-Hydro ensemble simulations in high mountain environment: Impact of boundary layer- and lateral flow parameterizations on land-atmosphere interactions. *Climate Dyn.*, **59**, 1355–1376, <https://doi.org/10.1007/s00382-021-06044-9>.
- Zhou, C., P. Zhao, and J. Chen, 2019: The interdecadal change of summer water vapor over the Tibetan Plateau and associated mechanisms. *J. Climate*, **32**, 4103–4119, <https://doi.org/10.1175/JCLI-D-18-0364.1>.
- Zhou, X., K. Yang, L. Ouyang, Y. Wang, Y. Jiang, X. Li, D. Chen, and A. Prein, 2021: Added value of kilometer-scale modeling over the third pole region: A CORDEX-CPTP pilot study. *Climate Dyn.*, **57**, 1673–1687, <https://doi.org/10.1007/s00382-021-05653-8>.

Copyright of Journal of Climate is the property of American Meteorological Society and its content may not be copied or emailed to multiple sites or posted to a listserv without the copyright holder's express written permission. However, users may print, download, or email articles for individual use.